LOCALIZED FLOW MODIFICATION TO INCREASE POWER CAPTURE OF A SMALL-SCALE FLOATING UNDERSHOT WATERWHEEL

by

Sullivan Hess

A Thesis Submitted to the Faculty of

the College of Engineering and Computer Science

in Partial Fulfillment of the Requirements for the Degree of

Master of Science

Florida Atlantic University

Boca Raton, FL

December 2020

LOCALIZED FLOW MODIFICATION TO INCREASE POWER CAPTURE OF A SMALL-SCALE FLOATING UNDERSHOT WATERWHEEL

by

Sullivan Hess

This thesis was prepared under the direction of the candidate's thesis advisor, Dr. Manhar Dhanak, Department of Ocean and Mechanical Engineering, and has been approved by all members of the supervisory committee. It was submitted to the faculty of the College of Engineering and Computer Science and was accepted in partial fulfillment of the requirements for the degree of Master of Science.

SUPERVISORY COMMITTEE:

Manhar Dhanak, Ph.D.
Thesis Advisor

Pierre-Philippe Beaujean
Pierre-Philippe Beaujean (Dec 2, 2020 09:54 EST)

Pierre Phillipe Beaujean, Ph.D.

Siddhartha Verma (Dec 2, 2020 10:02 EST)

Siddhartha Verma, Ph.D.

Manhar Dhanak, Ph.D.
Chair, Department of Ocean and Mechanical Engineering

Stella Batalama, Ph.D.
Dean, College of Engineering and Computer Science

Robert W. Stackman Jr., Ph.D.
Dean, Graduate College

December 3, 2020
Date

ACKNOWLEDGEMENTS

I would like to thank my advisors, fellow researchers, and family for making this journey possible. The knowledge and experience I have gained along the way will serve me well in the years to come, and I have your support to thank for it.

ABSTRACT

Author:	Sullivan Hess
Title:	Localized Flow Modification to Increase Power Capture of a Small-Scale Floating Undershot Waterwheel
Institution:	Florida Atlantic University
Thesis Advisor:	Dr. Manhar Dhanak
Degree:	Master of Science
Year:	2020

The goal of the work described in this thesis is to design a flow augmentation device to increase the power capture and efficiency of a small-scale floating Under-Shot Water Wheel (USWW) currently being developed by Florida Atlantic University research funded by the U.S Department of Energy. The flow concentrator subsystem is intended to maximize the kinetic energy extracted by the marine hydrokinetic (MHK) energy collection device through modification of the local flow field across the capture plane. The primary objective is to increase the velocity and/or rate of mass inflow through the turbine through inserting a streamlined body in the region of interest. By utilizing the resulting flow field to increase hydraulic forcing on the waterwheel blades, the torque and/or RPM of the USWW can be increased. Based on experimental testing in the FAU wave tank at 1:5 prototype scale (280 mm wheel diameter) the flow concentrator was shown to produce an increase in device power coefficient of 17-55% measured over a velocity range of 0.16-0.45 m/s.

LOCALIZED FLOW MODIFICATION TO INCREASE POWER CAPTURE OF A SMALL-SCALE FLOATING UNDERSHOT WATERWHEEL

LIST OF TABLES

LIST OF FIGURES

LIST OF EQUATIONS:

NOMENCLATURE

WAM-V	Wave Articulating Modular Vessel
MHK	Marine Hydro-Kinetic
WEC	Wave Energy Converter
ASV	Autonomous Surface Vessel
OTEC	Ocean Thermal Energy Conversion
CFD	Computational Fluid Dynamics
ADCP	Acoustic Doppler Current Profiler
USWW	Under-Shot Waterwheel
P_{th}	Theoretical Power / Available Power [W]
P	Mechanical Power / Measured Power Output [W]
C_p	Power Coefficient
a	Induction Factor
A	Device Area / Capture Area / Swept Area [m^2]
U	Current Flow / Water Velocity [m/s]
T	Mechanical Torque on Shaft / Measured Applied Torque [Nm]
λ / TSR	Tip Speed Ratio
α/AOA	Angle of Attack [deg]
R	Radius of USWW [m]
ω	Angular Velocity [rad/s]
ρ	Water Density [kg/m^3]
L	Characteristic Length [m]
Re	Reynold's Number

Fr	Froude Number

INTRODUCTION

Research at Florida Atlantic University funded by the Department of Energy aims to develop a mobile recharging station for coastal and offshore drone use. This offers the benefit of not only extending the flight duration for drone missions but also increasing their travel range offshore. One major consideration for a remote drone charging station is its power supply. Grid connections, while preferable for land-based operations, are impractical for offshore applications, particularly due to the high cost of underwater power transmission cables [21]. A large battery bank on site provides another possible solution; however, the amount of power that can be stored on-site is finite and will need to be replenished as drones extract power from the system. Therefore, it is beneficial to implement a means of power capture on-site to recharge the landing pad's power supply.

Several methods of power capture could be considered for coastal and off-shore operations including photovoltaic power cells (solar panels), small scale wind turbines and in-stream marine hydrokinetic (MHK) energy devices. While solar and wind energy technologies are highly developed, their dependence on cyclical resources leads to the issue of dead zones in power production. Solar panels cannot produce power during the night or on very cloudy days, and local wind resources can vary greatly especially at low altitudes, providing highly inconsistent, unpredictable power resources in many coastal areas. [21] This obstacle leads to the evaluation of alternative sources of energy in the field of marine renewable energy devices.

The current technology in marine renewable energy devices can be divided into three major categories: Wave Energy Converters (WECs), Ocean Thermal Energy Conversion (OTEC) systems and in-stream Marine Hydrokinetic (MHK) devices. The size of an OTEC plant is dictated by the

extremely large heat exchangers that are required due to the relatively low temperature gradient available to them, making this method impossible to apply on a small autonomous surface vessel (ASV). [21] WECs require a significant wave resource in order to operate and such a resource would exclude the operation of the ASV as excessive motion caused by rough sea states would not allow for the drones to land safely or maintain position on the charging pad. Furthermore, the relatively low efficiencies of most WECs (10-15%) means that an array of devices is typically required to consistently provide power. [21] In-stream hydrokinetic devices offer the benefits of scalability and higher efficiency than either OTEC or WEC systems. For this reason, in-stream MHK devices are selected for evaluation of their suitability for power production on the ASV charging platform.

In-stream Marine Hydrokinetic devices rely on a consistent and predictable resource: tidal and ocean current flow. The tidal cycle provides two "capture periods" where the water velocity is at its highest, one around each peak tide. In many coastal areas and channels, this tidal flow can range from 0.5-2 m/s. [21] Furthermore, this tidal flow is extremely predictable, making it a reliable power source for well-planned missions. Ocean currents such as the Gulf Stream Current offer the potential for these systems to harness power farther offshore in certain locations, eliminating the need for costly transmission cables.

The power output of in-stream MHK devices is primarily driven by their size, efficiency (power coefficient), and flow speed or current resource. Typically, these systems are designed to be permanently moored and operate in a specific location. By characterizing a local resource with an acoustic doppler current profiler (ADCP) the system can be optimized for maximum power production at the chosen site. A major challenge for this project is the desire for the system to be mobile, therefore operating in a variety of resource locations, each with their own current velocity distribution. A typical current velocity considered "sufficient" to produce meaningful power is >1 m/s. This system will need to function in a low flow velocity environment, with a target flow speed

of 0.5 m/s. The small size of the ASV platform provides another limiting factor for the power production of the system in the form of a physical limitation of device size based on vessel payload. The Wave Articulating Modular Vehicle (WAM-V) which will serve as the vessel platform has a maximum total payload of approximately 350 lbs, (158.6 kg) which is further limited by the presence of other onboard components so that the maximum allowable weight for the MHK system cannot exceed 140 lbs. (63.5 kg)

Due to the limitations on device size and current velocity, efforts are made to maximize the efficiency of the power capture device. One such adaptation which will be included in the system design is the use of a flow augmentation device, like the diffusers often used on small scale wind turbines. These devices make use of fluid dynamics principles in order to increase the flow velocity locally across the rotor plane. Three MHK device types are being considered for the purpose of providing power to the mobile drone recharging station: horizontal axis rotor, a vertical axis turbine, and an undershot water wheel. The work and findings presented in this report will be focused on developing a flow augmentation system specifically for the undershot waterwheel, as this has not been thoroughly investigated by prior research efforts.

BACKGROUND

Basic Energy Conversion Principles

The maximum amount of power theoretically available within a moving fluid stream is given by:

$$P_{th} = \frac{1}{2}\rho A U^3 \quad (1)$$

The mechanical power that can potentially be extracted from a moving fluid stream is given by the following equation:

$$P = \frac{1}{2}\rho A C_p U^3 \quad (2)$$

Where ρ = fluid density, A = device swept area, C_p = power coefficient, and U = inlet flow speed. The power coefficient represents the ratio of power captured by the device to the total available power within the flow stream.

$$C_p = P/P_{th} \quad (3)$$

The power coefficient can also be represented in terms of the axial induction factor, a, which describes the fractional decrease in flow speed between the free stream and the rotor plane [18] as seen below in Equations 4 & 5.

$$a = \frac{U_1 - U_2}{U_1} \quad (4)$$

$$C_p = 4a(1-a)^2 \quad (5)$$

By taking the derivative of this power coefficient relation with respect to the axial induction factor and setting it equal to zero (ie. $dC_p/da = 0$), the theoretical maximum for the power coefficient of an ideal open rotor is obtained. This is known as the Betz limit: $C_{pmax} = 16/27 = 0.593$, and it essentially means that there is only so much obstruction that can be imparted on the free stream before the fluid simply moves around the turbine rather than through the rotating system. [18] The power coefficient for a given device varies greatly with the turbines tip speed ratio (λ or TSR),

which represents the ratio of the tangential speed at the tip of the blades to the upstream velocity. The TSR can be shown mathematically by Equation 6.

$$\lambda = \frac{\omega R}{U_\infty} \quad (6)$$

Where ω = angular velocity (rad/sec), R = blade radius, and U_∞ = the upstream velocity. The various turbine types, including horizontal axis, vertical axis, and crossflow turbines each have an optimal TSR dictated by device type and number of blades as discussed in Multon's text, *Marine Renewable Energy Handbook*. [21] Any lift-based device will have a TSR > 1 while any drag-based device will always have a TSR < 1. The Betz limit discussed above can however be exceeded using a duct/diffuser to augment turbine performance. It can be seen by the above relations that the largest increase in power can be achieved by increasing the cubic velocity term, for example an increase in flow velocity by a factor of 2.0 results in an equivalent increase in power by a factor of 8.0. Additionally, based on the technology review conducted by Sornes [29], most MHK devices in production today have a minimum velocity requirement, or start-up speed of approximately 0.5 - 0.6 m/s, meaning that below this flow speed they cannot operate. In order to overcome this obstacle, a flow augmentation system is an attractive option.

Waterwheel Design Overview

The Under-Shot Water Wheel (USWW) has been identified as the most well suited MHK device type for use on the mobile drone recharging station. Its primary benefits when compared to Horizontal and Vertical axis turbines include low submergence allowing operation in any location, smaller moment arm/lower mounting point to ensure vessel stability and low startup speed due to non-lift-dependent operation. [27] Free-stream USWWs operate in uncontrolled, un-dammed free-surface flows; because of the unconstrained movement of the free surface it is difficult to determine a priori or control the fluid velocity at the rotor plane, complicating the search for a blade geometry that facilitates smooth entry and exit from the water. In an effort to develop a more accurate method

for modelling such energy conversion systems and to quantify major performance characteristics, a study was conducted by Olivier, et al. [7] using 2D CFD analysis on induvial blades and experimental verification using a 0.3 m diameter by 0.25 m wide wheel. This method allows for the identification and quantification of observable phenomena such as entry splash, departure water pickup, water build-up, and interference between blades. This study examined the effect on efficiency of varying wheel depth, tip speed ratio, tip angle, and number of blades. The results of this study indicate that deeper wheels, slower wheels, and wheels operating in faster flows offer higher total power delivery, at the cost of decreased efficiency and higher oscillations in power delivery. Increased depth and decreased tip speed ratios result in water build-up immediately upstream of the wheel, with generally detrimental effects on the power output. [7] The energetic cost of water pick-up by the departing blade largely exceeds the benefit of a smoother entry into the water brought by tilting the blade tip in the direction of rotation. An increased number of blades results in higher, smoother power delivery, until interference effects caused by insufficient blade spacing reverse the trend. Within the range of parameters investigated, the results suggest that a rotor with a small diameter would work optimally with fewer blades and deeper immersion; while an emphasis on smooth power delivery for a limited wet frontal area points towards a wheel with more blades and higher rotor diameter. Selecting an optimum configuration requires a formulation of constraints reaching beyond fluid mechanics, considering consequences associated with rotor size, number of blades, or oscillating power delivery as they pertain to a given system.

Flow Augmentation and Energy Conversion Devices

There are two basic tactics implemented to augment the performance of wind and marine current turbines: ducts and diffusers. The technology review conducted in [29] on the state of technology in small scale river hydrokinetic turbines suggests that the presence of a duct or diffuser can greatly impact the performance of a turbine. These specially designed structures elevate the energy density of a water stream as it passes through the turbine rotor, increasing the possible total power capture

significantly. Sornes [29] also suggests that this augmentation may serve to regulate the speed of the rotor and reduce problems caused by low-speed drive train design as well. Ducts and diffusers share the same goal of increasing the mass flow and fluid velocity across the rotor plane, however they accomplish this in different ways. A duct aims to direct the flow into the turbines swept area by a converging inlet ring or ramp, while a diffuser creates a negative pressure zone at the rear of the turbine with a diverging outlet ring or ramp.

A study conducted by Chihaia, El-Leathey, Cîrciumaru, and Tănase [5] performed experiments on a small-scale hydrokinetic turbine with a horizontal axis type rotor evaluating both converging and diverging shrouds. They tested their turbine at various positions relative to the shrouds. Their study found that use of the shrouds had a significant positive impact on the device output. Their work concluded that the best results were obtained using the divergent shroud with the rotor placed in front of the shroud, aligned with the upstream edge, noting maximum power generation of 11W at 300 RPM, compared to the 4W max at 230 RPM for their open rotor. [5]

Another study conducted by Ohya & Karasudani [23] investigated the performance of a compact brimmed diffuser on a small-scale wind turbine, also of the horizontal axis configuration. Their goal was to develop a diffuser that was more compact than the traditional long throat diffusers, which can be excessively large in comparison to the rotor diameter. This study determined that the presence of a brim near the outlet increased the diffusers performance, more so than increasing the throat length, leading to the conclusion that a more compact device could be very effective for small scale devices. The field data obtained by this study includes a power coefficient Cp = 1.0 calculated based on the rotor area (A) only, if the swept area due to the brim diameter (*Dbrim*) at diffuser exit (*A**) is considered, the output coefficient becomes *Cp** = 0.48–0.54 for the compact wind-lens turbine. While lower than it appears initially, the power coefficient of this design is still larger than the power coefficient of the open wind turbines, which was measured to be around 0.4.

[23] Meaning that this wind-lens diffuser results in a more efficient turbine than the un-augmented type even when the total brim area is considered.

A study by Khan et al. [12] which provides an analysis of the state of small scale marine hydrokinetic turbine technology contains a description of several augmentation schemes that have been implemented for both horizontal and vertical axis turbines. The various augmentation channel designs discussed in this study and considered for application to the waterwheel include: Hybrid (Curvilinear & Rectilinear) Channel and Multiple Hydrofoil Diffusers for Vertical axis turbines and Annular Ring and Rectilinear Diffusers (with and without a brim) for Horizontal axis turbines.

An experimental study conducted by Mannion et al. [17] investigated the effectiveness of a bluff body type flow acceleration device on a vertical axis turbine. Within this study, testing of the tidal stream device was conducted at 1:40 scale with a bluff body diameter of 0.4m and turbine diameter 0.15m and subsequently at 1:20 scale with a bluff body diameter of 1.64m and turbine diameter 0.6m, using scale factors based on the device entrance area. As is to be expected, the measured velocity was found to be highest at the widest point of the bluff body, reaching an increase factor of 2.0 for the bluff body alone. The frictional boundary layer was visually observed to be approximately half the width of the bluff body; nevertheless, flow acceleration in excess of 60% above the free stream velocity was recorded with the turbine in place. The peak mechanical efficiency of 40% (normalized for total device area) achieved in this study is slightly higher than many other vertical axis turbines, which typically reach efficiencies of 25-32% [17] suggesting that the bluff body acceleration scheme is another effective method.

Hydrofoil Principles

The geometry of the waterwheel and horizontal axis turbine are too dissimilar for a device like the annular diffuser to be considered; however, a design which incorporates aspects of the Curvilinear/Multiple Hydrofoil channels will likely be well suited to the floating waterwheel. The

bluff body style accelerator designed in [17] seems to be an effective tactic, however, is quite large in relation to the turbine itself. Since it is important to minimize the weight and induced drag force of the system under development, a more streamlined augmentation channel is desired. Hydrofoil shapes appear to be a good candidate for the purpose of providing flow acceleration to the MHK collector without inducing excessive drag. These specialized shapes are designed with profiles that follow the fluid streamlines and can have a large impact on the surrounding flow field's velocity and pressure distribution. An outline of hydrofoil geometry as presented by Manwell, J. F., et al. *Wind Energy Explained: Theory, Design and Application* [18] is shown in Figure 1 below.

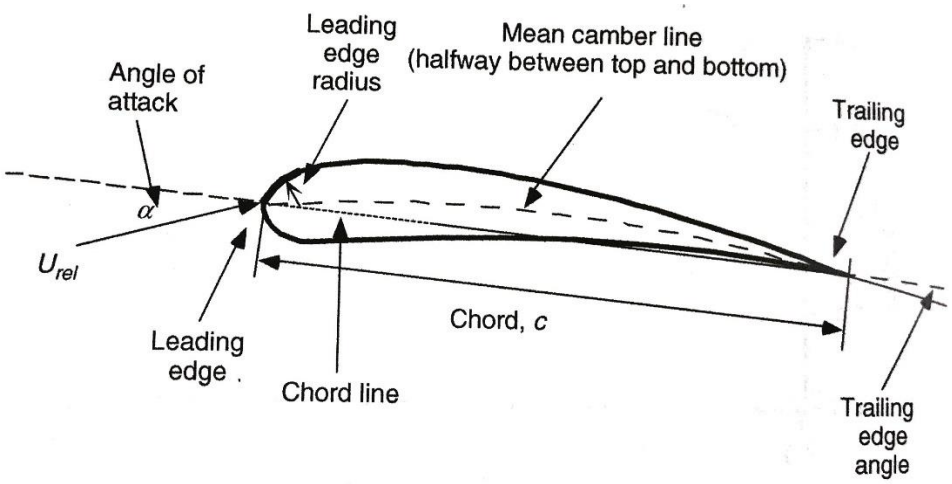

Figure 1: Foil profile dimensional characteristics and terminology, as presented by Manwell, J. F., et al. Wind Energy Explained: Theory, Design and Application [18]

This specialized geometry creates a pressure difference between the top or suction side of the foil and the bottom or pressure side when oriented at an angle, known as the Angle of Attack (AOA), relative to the oncoming flow stream. This pressure difference results in the force components illustrated in Figure 2 below. The ratio of these forces can be described as dimensionless coefficients known as lift and drag coefficients.

$$C_l = \frac{L/l}{\frac{1}{2}\rho U^2 c} = \frac{Lift\ force/unit\ length}{Dynamic\ force/unit\ length} \quad (7)$$

$$C_d = \frac{D/l}{\frac{1}{2}\rho U^2 c} = \frac{Drag\ force/unit\ length}{Dynamic\ force/unit\ length} \quad (8)$$

The higher the lift to drag ratio of a foil shape, the greater the pressure difference between the pressure and suction sides, and therefore the higher the fluid velocity that can be induced over the top of the foil. [18]

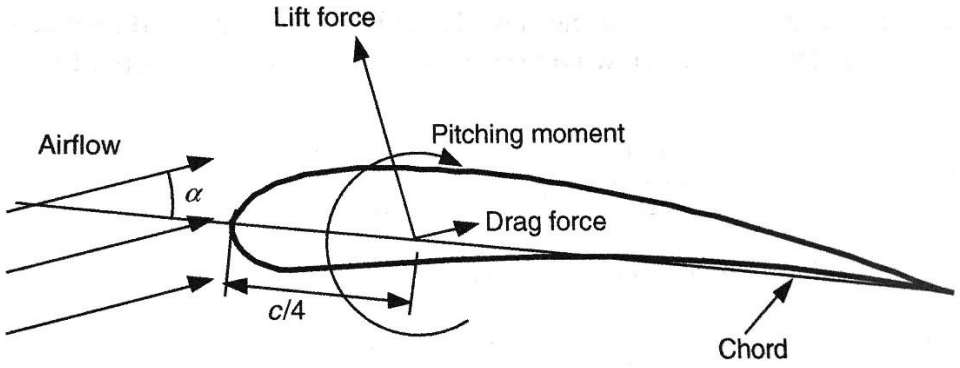

Figure 2: Forces developed by a foil shape, courtesy of Manwell, J. F., et al. Wind Energy Explained: Theory, Design and Application [7]

The pressure variations observed in the flow around a hydrofoil can be understood using Bernoulli's principle, which states that when friction losses are neglected, the sum of dynamic and total pressure must remain constant

$$P + \frac{1}{2}\rho U^2 = Constant \quad (9)$$

As the flow moves along the rounded leading edge to the top/suction side of the foil, it accelerates, causing a negative pressure gradient, decelerating as it approaches the trailing edge and causing a positive pressure gradient. The variation in these pressure gradients along the foil surface is key to generating flow acceleration along the upper surface.

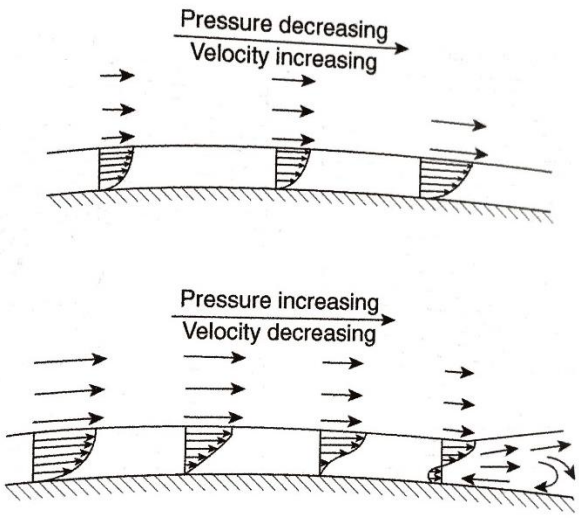

Figure 3: Boundary layer pressure gradients, for suction side (top) and pressure side (bottom) of the foil profile, as presented by Manwell, J. F., et al. Wind Energy Explained: Theory, Design and Application [18]

An important factor which heavily impacts foil performance and scalability is the Reynold's number. Sometimes called the non-dimensional velocity, the Reynold's number is a dimensionless number describing the ratio of inertial forces (ρUL) to viscous or friction forces (μ) within a given fluid flow. [3] It can also be interpreted as the ratio dynamic pressure (ρU^2) to shearing stress ($\mu U/L$). The Reynold's number can therefore be expressed in the following ways:

$$\mathrm{Re} = \rho\, U\, L / \mu = \rho\, U^2 / (\mu\, U / L) = U\, L / \nu \qquad 10$$

Where: Re = Reynolds Number (non-dimensional), ρ = fluid density (kg/m^3), U = velocity based on the actual cross section (m/s), μ = dynamic viscosity (Ns/m^2), L = characteristic length (m), $\nu = \mu / \rho$ = kinematic viscosity (m^2/s)

The lift and drag characteristics of specific foil profiles can be examined over a range of angles of attack and various Reynold's numbers, with different geometric characteristics leading to differences in performance. For example, some foil profiles have good lift/drag characteristics (ie. high ratio of lift to drag) in a low Reynold's number flow regime, while others may be better suited for use in very high Reynold's number flow. The database found on *Airfoiltools.com* [14] provides

an extensive library of foil shapes along with performance characteristic curves generated using X-Foil code, typically over a range of -15°/+20° and Reynold's numbers ranging from 50,000 – 1,000,000+.

Computational Fluid Dynamics

As discussed in detail in Zikanov's textbook *Essential Computational Fluid Dynamics*, [35] the rapid development of computers and their ability to perform millions of arithmetic operations very quickly has given rise to the field of Computational Fluid Dynamics (CFD). Within the last 20-30 years, this field has expanded from occasional use of highly specialized custom codes to a widely available tool for a variety of engineering practices. These simulations are often conducted as a supplement to or replacement for prototype testing and other design techniques. The market for commercial programs is divided into several prominent brands including FLUENT, CFX, STAR-CD, OpenFOAM, COMSOL, PolyFlow etc. While their capabilities and user interfaces differ slightly, they all operate on the basis of numerically solving partial differential equations, with various physical and turbulence models included and modules for mesh generation and post processing of results. [35] These numerical solvers are based on the conservative laws of classical physics: the law of conservation of mass, Newton's 2nd Law of motion, the first law of thermodynamics and equations of state. These laws provide the basis for numerical analysis of any continuous medium (solid or fluid) consisting of many finite volume elements.

The first relevant governing equation is the conservation of mass, or the continuity equation:

$$\frac{D\rho}{Dt} + \rho\Delta \cdot V = 0 \qquad 11$$

Which states that when considering a fluid element with a given volume, this element is always comprised of the same molecules and therefore must maintain a constant mass, ie. mass cannot be created nor destroyed. This relation can be further simplified in the case of incompressible flows:

$$\Delta \cdot V = 0 \quad (12)$$

The next relevant governing equation is the conservation of momentum, or Newton's 2nd law:

$$F = ma \quad (13)$$

This is one of the most fundamental equations in all of physics, which states that the force acting on an object must be equal to the product of its mass times its acceleration. By substituting the material derivative, this relation can be expressed for cartesian coordinates as:

$$\rho \frac{Du}{Dt} = \rho \left[\frac{\delta u}{\delta t} + u\frac{\delta u}{\delta x} + v\frac{\delta u}{\delta y} + w\frac{\delta u}{\delta z}\right]$$

$$\rho \frac{Dv}{Dt} = \rho \left[\frac{\delta v}{\delta t} + u\frac{\delta v}{\delta x} + v\frac{\delta v}{\delta y} + w\frac{\delta v}{\delta z}\right]$$

$$\rho \frac{Dw}{Dt} = \rho \left[\frac{\delta w}{\delta t} + u\frac{\delta w}{\delta x} + v\frac{\delta w}{\delta y} + w\frac{\delta w}{\delta z}\right] \quad (14)$$

These forces in general can be divided into two types, body forces and surface forces. Any force which acts directly on the fluid mass and originates from a remote source can be considered body forces. Gravity is a prime example of a body force, as well as electric or coulomb forces, magnetic forces and centrifugal forces when considering a rotating reference frame. [35] Surface forces consist of pressure and friction forces acting between two adjacent fluid elements or between a fluid element and a boundary wall. These forces can be represented as the divergence of a symmetric 3x3 stress tensor (τ). This stress tensor can be separated into two parts, the isotropic pressure, which is always present, and the viscous of friction component, which is only present in a moving fluid. [33] These pressure body forces are manifested according to Equation 15, where F is the body force (N), P = Pressure (Pa) and A = Area (m^2)

$$F = P \, x \, A \quad (15)$$

Boundary Conditions

CFD numerical studies must consider a finite domain which is representative of the area of interest to a study. These boundaries can sometimes represent a natural boundary such as a rigid wall, however sometimes it is necessary to implement artificial boundaries for pressure, temperature, velocity, etc. to satisfy computational requirements. [9] For example, when considering the flow surrounding an ocean current turbine, it would be unrealistic to attempt to model the entirety of the ocean. Even though no physical boundary may be present, one must be defined to narrow the focus of the analysis on the area of prime interest. The proper definition of appropriate boundary conditions is therefore profoundly necessary setting up a correct CFD simulation.

Rigid Wall Boundaries

At a rigid wall boundary, the velocity constraint differs when considering inviscid flows ($\mu = 0$) compared to viscous flows ($\mu \neq 0$). For any viscous flow, where friction is considered, the no slip condition must be applied at the walls meaning that the flow velocity at the boundary wall is zero. For inviscid flow problems the free slip condition should be applied so that the velocity in the boundary layer is unaffected by the presence of the wall. [33]

Inlet and Exit Boundaries

If the computational domain considered has open or artificial boundaries, as nearly always is the case, special conditions must be set. A common method is to prescribe a velocity, temperature or pressure across that boundary. Turbulent parameters must also be considered here if they are included in the analysis. [31] It is important that these boundaries are considered and defined properly, as predictions for what occurs outside the computational domain boundaries is impossible. Furthermore, incorrect artificial boundary definitions can impact the physical phenomena observed within the computational domain, causing invalid solution results.

Incompressible Flow

In incompressible fluid flow, the density, viscosity and heat conductivity of the fluid are considered to be constant. The Navier-Stokes and continuity equations which govern incompressible flow can then be shown as:

$$\rho \frac{DV}{Dt} = -\nabla p + \mu \Delta^2 + \rho f \quad 16$$

$$\nabla \cdot V = 0 \quad 17$$

When considering incompressible flow, the pressure field must satisfy:

$$\nabla \cdot (\nabla p) \equiv \nabla^2 p = \rho \nabla \cdot [f - N(V, V)] = \rho \nabla \cdot F \quad 18$$

In an incompressible flow regime, the pressure field across the entire fluid domain reacts instantaneously to any perturbation, however localized. Several methods can be used to perform this non-trivial simultaneous solution of the momentum and pressure equations. [6]

Turbulence

Most fluid flow examples found in nature are turbulent. Turbulent flow displays three major characteristics: irregularity, three-dimensionality and time dependence. [8] In dealing with turbulent flow, it is commonplace to define a mean flow velocity which is the statistical average of the velocity field which contains variations. Turbulent flow, while seemingly random, is still in fact represented by a solution to the Navier-Stokes equation, following a predictable evolution determined by initial and boundary conditions. Turbulence can be understood by the concept of energy cascade introduced by L.F Richardson in 1922. [35] Large flow structures called eddies or vortices are constantly being generated by hydrodynamic instabilities within the flow. These eddies are unstable themselves, causing smaller vortices, which in turn break down to even smaller eddies. This continues until the kinetic energy originally present within the flow is completely dissipated as heat. Turbulent flow displays a high level or pseudo randomness caused by small perturbations constantly being added to the flow field and enhanced over time exponentially. In the case of practical CFD applications, these constantly unstable flows are treated as truly chaotic. When

dealing with turbulent flows in CFD analysis, there is a very important distinction between simulation and modelling methods. In the case of the simulation approach, such as direct numerical simulation (DNS) and large eddy simulation (LES), the unmodified Navier-Stokes equations are solved, providing a complete picture of a time dependent flow field. The drawback of this method is the excessively fine grid or mesh required to capture the small length scale of the turbulent eddies, making it an inefficient and impractical solving method in most cases. [35] Modelling on the other hand recasts the system of equations to represent mean flow quantities such as velocity, pressure, Reynold's stresses etc. This Reynolds Averaged Navier stokes (RANS) method can be less accurate due to the approximations made but is highly computationally efficient. The RANS method is the most widely utilized method, with various models built into most available CFD programs. [14] Of these RANS methods, the k-Epsilon ($k - \varepsilon$) method is the most widely implemented. This model consists of two partial differential equations and an algebraic expression for eddy viscosity. The equations for K and Epsilon must be solved simultaneously with the mass and momentum conservation equations. The model contains five constant parameters which have been determined through previous experimental results and DNS to fine tune the model.

Computational Domain: Grids and Meshing

A properly constructed computational grid or mesh is vital to accurate, efficient and robust CFD analysis. These grids can be uniform Cartesian or non-Cartesian unstructured meshes. The general principles of CFD analysis discussed previously are valid in both cases. One major consideration in selecting a mesh type is the geometry of interest. In many cases curved faces are present, which leads to difficulty in implementing a Cartesian grid as the curved surface would instead be represented as a sort of staircase of grid points. In some cases, a curvilinear coordinate system can be implemented. It is often the case that a uniform grid is not desirable because the gradients of solution variables may be significantly different in one area of the domain than another. For example, mean velocity and turbulence display very large gradients in boundary layers, conversely

these gradients can be quite small far from boundary layers. In these cases, it is beneficial to implement an unstructured mesh with a finer grid near boundary layers to accurately capture the solution variables and a courser mech away from boundaries to reduce computational effort. It is therefore typically desired to apply an unstructured grid to the computational domain and then apply finite element or finite volume discretization. [24] This method offers three major advantages: applicability to a variety of arbitrary geometries, high level of flexibility and control of grid parameters such as cell size and shape, and the existence of mesh generation algorithms in most commercial programs. [15]

Experimental Testing and Scaling Procedures

Scaled physical models are used in science and engineering to approximate real-world systems. Since it is often impossible to directly test a full-scale system, various scaling procedures have been developed to ensure the accuracy of scale model and prototype testing. The principle of dynamic similarity allows for geometrically scaled systems to be dynamically identical if certain nondimensional parameters are matched. [20] In the case of fluid systems, the most important nondimensional parameter is often the Reynold's number, Re, which quantifies the relative effects of inertial forces and viscous forces on the flow physics [Eqn. 10]. The other prominent scaling method often implemented for systems that pierce the free surface is based on matching the Froude number (Eqn. 19 below) which represents the ratio of the flow inertia to the external field forces, ie the force due to gravity. Matching both the Froude and Reynold's number is often not possible for a scaled model in a given fluid regime since the Reynold's and Froude numbers scale differently according to length scale. The applicability of these methods varies by testing conditions and objectives, making careful consideration and selection of proper scaling method imperative.

Reynold's Scaling

This scaling method is based on achieving similitude between full scale and prototype scale Reynold's numbers. Previous research efforts [30] examining the Reynold's number dependence

of the performance of various turbine types suggests that hydrokinetic turbines typically display strong Reynold's number dependence for Re $<10^5$. Table 1 below summarizes the expected Reynold's number range based on the geometry and flow conditions of the full and prototype scale using the chord length of the concentrator's NACA 4412 vertical foil as the characteristic length.

Table 1: Expected range of Reynold's numbers for prototype and full-scale flow conditions

Reynold's Numbers: Re = U*L/v		
Flow Speed (m/s)	Full Scale	Prototype Scale
0.1	75,896	15,179
0.25	189,741	37,948
0.5	379,482	75,896
1	758,964	151,793
1.25	948,705	189,741
2.5	1,897,410	379,482

Froude Scaling

This scaling method often implored in ship hydrodynamics and other surface piercing applications relies on matching of the Froude number for each condition. The Froude number (Fr) relation is given below:

$$Fr = U/\sqrt{(gL)} \qquad 19$$

Where: U is the free-stream velocity, g is the gravitational acceleration, and L is the characteristic length or model depth. There are three flow conditions as dictated by the Froude number's relationship to unity: sub-critical, critical, and super-critical flow.

Fr = 1 critical flow

Fr > 1 supercritical flow (fast rapid flow)

Fr < 1 subcritical flow (slow tranquil flow)

At critical flow, celerity equals flow velocity, meaning any disturbance to the surface will remain stationary. In subcritical flow, the flow is controlled from a downstream point and information is transmitted upstream, leading to backwater effects. Supercritical flow is controlled upstream and

disturbances are transmitted downstream. [3] Using the definition shown in Eqn. 19 above, the range of Froude Numbers to be expected for the full and prototype scales are summarized below. The maximum blade submergence for each case was used as the characteristic length/ model depth.

Table 2: Expected range of Froude numbers for prototype and full-scale flow conditions

Froude Fumbers: Fr = U/sqrt(gL)		
Flow Speed (m/s)	Full Scale	Prototype Scale
0.1	0.0476	0.1064
0.25	0.1190	0.2661
0.5	0.2380	0.5321
1	0.4759	1.0643
1.25	0.5949	1.3303
2.5	1.1899	2.6606

Selected Scaling Method

Based on comparison of the expected Reynold's and Froude number ranges, it was deemed more important to match the Reynold's numbers in this case. The Froude numbers achievable in the flow tank (with a max testing velocity of ~0.5 m/s) are exclusively sub-critical, with critical/super-critical flow not being reached until 2.5 m/s at the full scale. The range in Table 1 shows that the Reynold's numbers are directly correlated, with a linear relationship based on the 1:5 length scale ratio. Using this relationship, the testing results for measured power coefficient shall be scaled in order to predict full scale performance metrics. Using the method implored by Muller [20], the measured average power coefficient per tip speed ratio shall be scaled based on corresponding Reynold's number conditions.

APPROACH

CFD Analysis:

The commercial software ANSYS CFX was used to perform the preliminary CFD analysis required for this study. This program offers robust capabilities, with the ability to import geometry created in SolidWorks or other CAD software and a variety of post processing options for dissemination of the solution results. [2] It operates based on the principles outlined in the Background section as a finite element solver. A single fluid domain containing the concentrator under development was analyzed. This model contained the part geometry and surrounding fluid domain only, with appropriate inlet, outlet and wall boundaries. An unstructured tetrahedron 3-D mesh was applied to the fluid domain. The mesh applied to the domain was fine (small element size) near the concentrator surface to accurately capture the details of the boundary layers, and coarse (larger element size) far away from the part to minimize computational demands. This solution served to inform the selection of effective candidate shapes and subsequently verification of the level of flow acceleration induced by the concentrator profile. It also allows for measurement of the total drag force exerted by the surrounding pressure field on the hydrofoil shapes. A secondary simulation was originally proposed to model waterwheel performance, including a rotating domain and free surface; however, after examining the solutions obtained by this simulation, the conclusion was reached that CFD analysis was not the proper tool for this complex system. Issues with the air/water domain interface and initialization resulted in impossibly high torque outputs. and based on visual examination of the pressure, velocity and volume fraction contours other unidentified issues were certainly present. While some valuable knowledge and insight was gained into the use of ANSYS CFX software for complex external flow problems, the results from the split-domain rotating

frame of reference simulation were deemed unreliable and were omitted from the report; the setup and results are included in Appendix A. The remainder of the analysis regarding waterwheel and concentrator performance was conducted using prototype testing in the FAU wave tank.

Experimental Testing:

For the purpose of understanding of the concentrators impact on waterwheel performance based on measuring an increase in power coefficient, experimental testing yielded more robust results than the preliminary CFD analysis. 1:5 scale prototypes of the waterwheel, concentrator and WAM-V pontoons were fabricated and tested in the FAU wave-tank. Three different waterwheel prototypes were tested: V1 with 7 blades, followed by V2a/b with 9 and 11 blades respectively.

The key areas of interest for experimental testing are the accurate measurement of the applied torque at the waterwheel shaft and angular velocity (ω) or RPM of the wheel. The rotational speed and torque generated by the waterwheel determine the amount of mechanical power that it captures from the flow stream according to Equation 20 as shown below:

$$P_{mech} = T\omega \tag{20}$$

Where T = measured applied torque (N-m) and ω = angular velocity (rad/sec). By comparing the experimentally measured torque and RPM of the waterwheel both with and without the concentrator in place, its impact on power capture and efficiency can be directly measured.

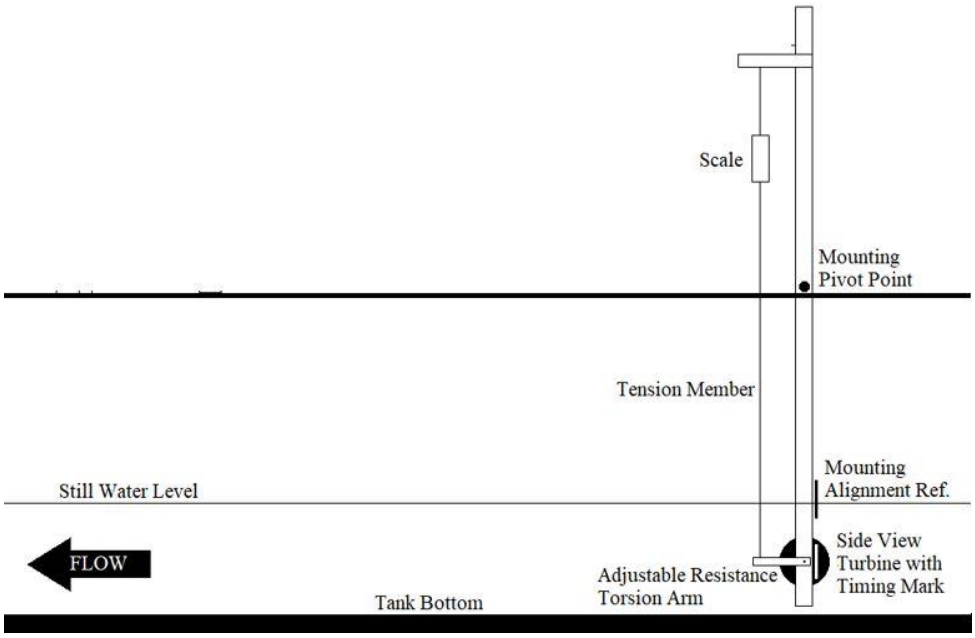

Figure 4: Tank testing apparatus to be used to measure the waterwheel torque and RPM in the FAU wave tank

The scale attached to the torsion arm will measure the waterwheel torque while the hall sensor and magnet shall be used to measure the angular velocity or RPM of the wheel. The torque and angular velocity measurements together will provide a direct measurement of mechanical power extracted by the MHK device.

FAU Wave Tank:

The flow tank at FAU's Sea Tech campus uses three electric motors to drive separate but coordinated impellers to push/pull the working fluid though the circulated plumbing. The controller for the motors uses frequency as its input, with a range of 0 - 60Hz. The flow velocity in the tank has been characterized for a static water depth of 54.8 cm. Since changing the depth results in a linear change in cross section, flows at other depths can be calculated using this information. The tank calibration results are shown in Table 3 below.

Table 3:Water velocity calibration table for the FAU wave tank over the tank motor controller range from 0-60 Hz

Tank Setting (Hz)	Calibration Depth (m)	Calibration Speed (m/s)	Testing Depth (m)	Testing Flow Speed (m/s)
10	0.584	0.075	0.406	0.108
20		0.125		0.180
30		0.190		0.273
40		0.250		0.359
50		0.300		0.431
60		0.350		0.503

V1 Prototype Design & Testing:

The first undershot waterwheel prototype was assembled from HDPE plastic endplates and aluminum sheet metal scoops sealed with white spray enamel. The V1 prototype has 7 blades, each with a a cord length of 101 mm. The wheel is positioned so that water does not overtop the blades except by wave action.

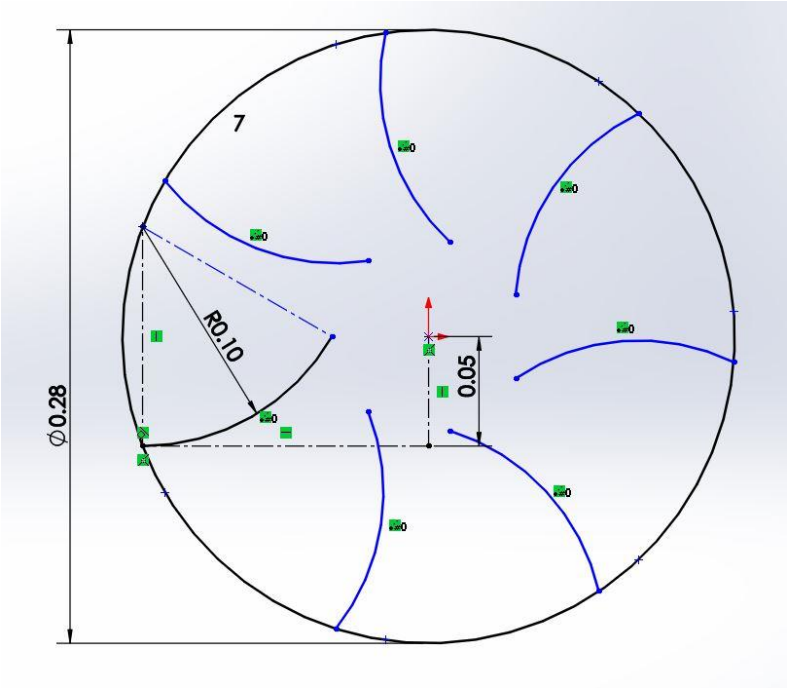

Figure 5 Blade geometry sketch for the 7-blade V1 waterwheel prototype; units shown in meters

Figure 5 above shows a side-view of the V1 wheel blade geometry sketch. The main condition which should be satisfied by the blade geometry is that the blades should be tangent to the waterline

when entering the water; if the blade entry angle is too large, a detrimental suction effect occurs as the “bowl” created by the blade is pulled into the water, while an insufficient angle results in diminished positive effects of the curved blades. The red marking seen in Figure 6 below serves as the reference for visually measuring RPM on recorded video files (for initial datasets collected prior to completing DAQ setup).

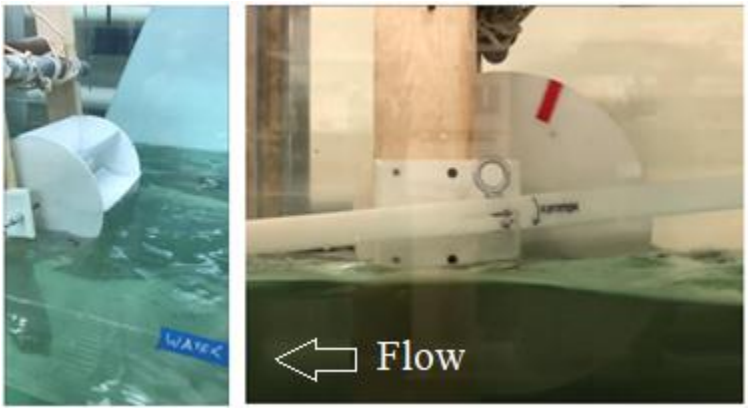

Figure 6: Waterwheel tank testing, unloaded RPM measurements and torsion-brake power measurements

V1 Flow Concentrator:

In searching for appropriate hydrofoil shapes, the resources found on airfoiltools.com [14] proved to be very useful. The database offers an extensive library of foil profiles, with coordinate files used to generate the foil shapes in Computer Assisted Drafting (CAD) programs and lift/drag polar plots for various Reynolds numbers. The performance curves are generated using Xfoil software over a range of -15/20° to +20° angles of attack (AOA/α). This provides curves of the lift, drag and added mass coefficients for a given foil profile, allowing for direct comparison of various candidate foils. The foil profiles selected at this stage for evaluation are the NACA 0018 and NACA 4412.

The NACA 0018 foil profile is a symmetric foil, meaning that it produces no lift at 0° angle of attack (AOA/α). This shape is one of the most widely used foil profiles, with predictable lift/drag characteristics over a wide range of Reynold’s numbers. The profile shape and details are shown below in Figure 7.

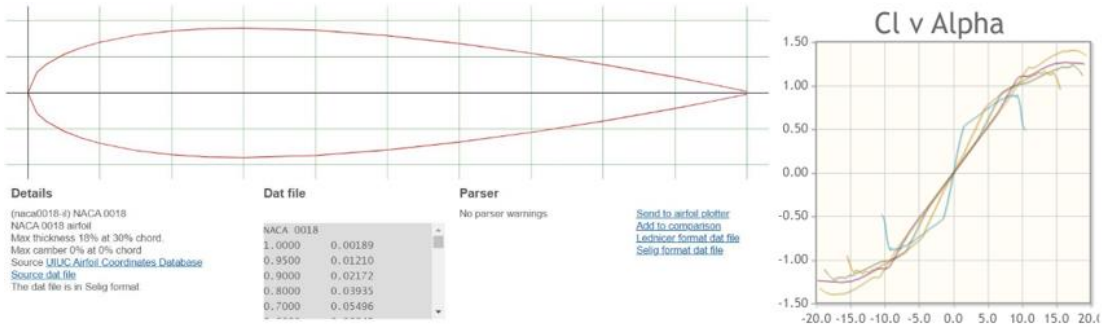

Figure 7: NACA 0018 foil shape and details (left), Lift coefficient curve (right)

The NACA 4412 profile was selected for comparison with the symmetric foil due to its performance at low Reynolds numbers (Re < 200,000). Because this foil has a curve, or camber, it will produce lift at 0° AOA.

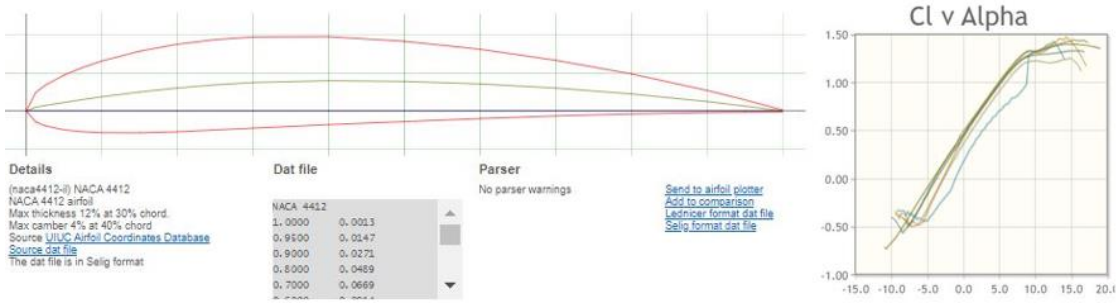

Figure 8: NACA 4412 foil shape and details (left), Lift coefficient curve (right)

The V1 flow concentrator prototype features the NACA 4412 wing and adjustable mounting side panels to test various positions. It was fabricated with foil support sections 3D printed at the FAU Sea Tech facility using a Tevo Tornado 3D printer and Ultamaker Cura slicing software, shown in Figure 9 below. The NACA 0018 wing will be fabricated in the same manner to be implemented in V2 prototype testing. The positioning of the concentrator relative to the wheel is an important factor in obtaining good performance, and therefore is investigated extensively during prototype testing.

Figure 9: Concentrator prototype (left/right) and 3D printed support section (middle)

The proposed configuration for initial testing of the waterwheel and concentrator consists of two clear acrylic support panels which will allow for observation of flow patterns through the device as well as adjustment of the bottom wing to test a range positions and orientations. After the optimal position is determined, the flat panels will be replaced with the NACA 4412 side wings and the NACA 0018 symmetric foil will serve as the bottom wing.

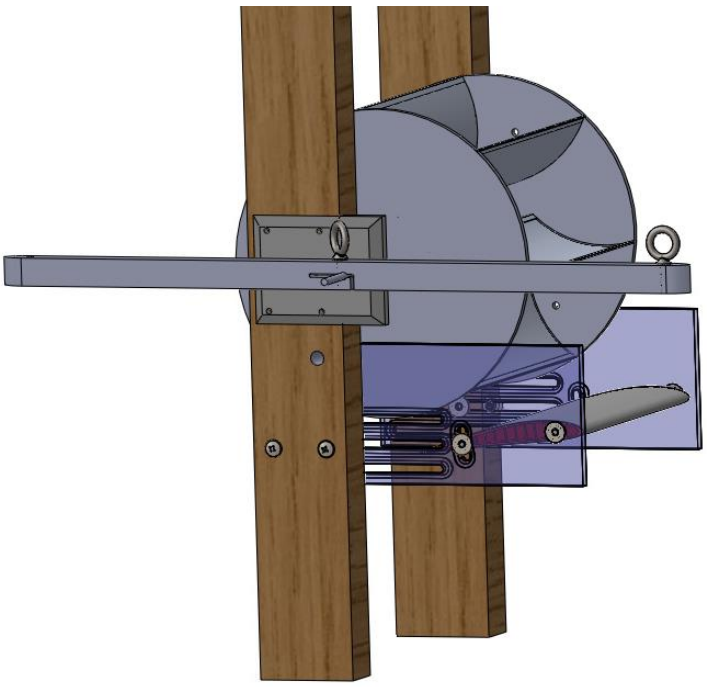

Figure 10: Testing assembly for waterwheel and concentrator, with adjustable mounting panels, bottom wing NACA 4412 foil and 7 Blade V1 Wheel

Based on the results of the V1 testing, modifications were made to the wheel to improve performance characteristics.

Preliminary Testing Positions:

15 different positions were investigated during the initial testing phase to determine the effects on performance of varying forward position, vertical position, and angle of attack of the concentrator wing. A positive angle of attack acts as the diffuser channel, while a negative angle of attack serves as a duct. The results of this testing phase will inform future testing in terms of prototype fabrication and placement relative to the MHK. The positions examined include:

- Full forward position, max height, +/-10° & Neutral angle of attack
- Full forward position, mid height, +/-10° & Neutral angle of attack
- Mid Forward Position, mid height, +/-10° & Neutral angle of attack
- Mid Forward Position, low height, +/-10° & Neutral angle of attack

- Rear Position, mid height, +/-10° & Neutral angle of attack

V2 Prototype Design & Testing:

After testing the 7-blade V1 Undershot Water Wheel (USWW) prototype, it became clear that device performance could be improved. The initial prototype reached a measured Power Coefficient Maximum (C_p max) of roughly 0.135 when submerged to 15% of the wheel diameter, with decreasing C_p max as submergence was increased. This led to the realization of insufficient power capture; a larger area and higher efficiency would be required to make the full-scale device viable. The side-view profiles in Figures 12 & 13 illustrate the blade geometry for the 9- and 11-blade configurations. The alterations to the design were made based on the findings presented by [7] as well as observations made during the initial rounds of testing on the V1 7-blade device.

V2 Waterwheel:

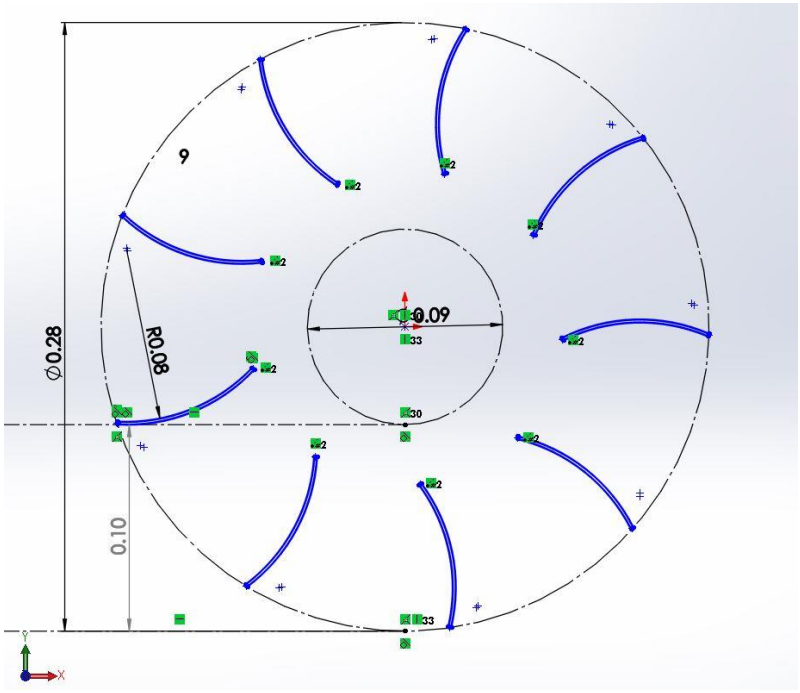

Figure 11: Blade geometry sketch for the 9-blade V2 waterwheel prototype; units shown in meters

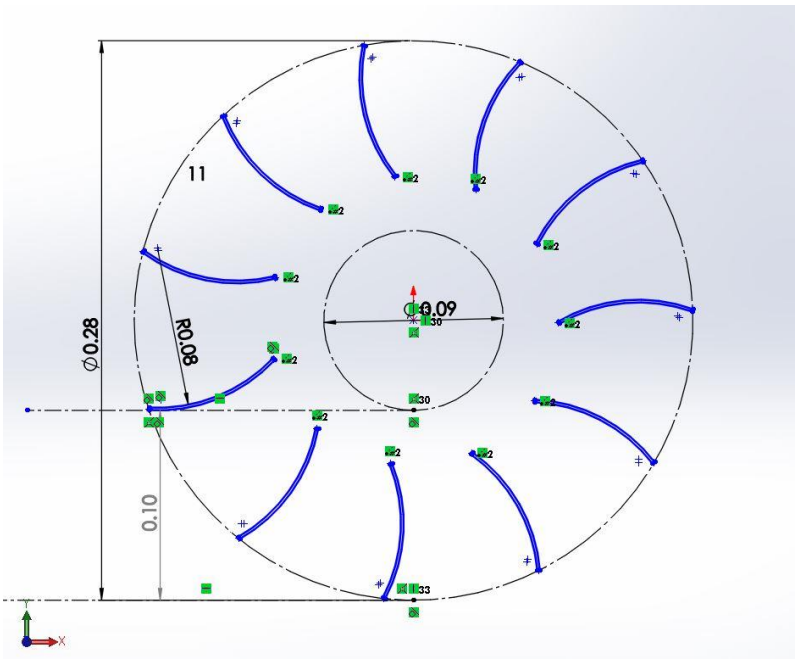

Figure 12: Blade geometry sketch for the 11-blade V2 waterwheel prototype; units shown in meters

When re-evaluating the waterwheel blade geometry, the force analysis method presented by Quaranta [27] was useful in determining blade angles which led to beneficial force characteristics. By examining the force components of lift and drag exerted on a single blade during its rotation stroke within the water, an entry angle of approximately 165° was recommended. The V2 prototypes accommodate a larger capture area by submerging the wheel to 33.3% of its diameter resulting in an increase in capture area of 106% from 121.8 cm^2 to 252 cm^2. The cogging effect observed while testing the V1 prototype; where the angular velocity of the wheel oscillated throughout its rotation based on blade position, was addressed in the redesigns. To reduce this effect, the V2a and V2b prototypes increased the number of blades to 9 and 11 blades respectively. The arc length of the blades was also reduced so that water can overtop the blades when they reach the bottom of the rotation stroke. It is likely that performance will be improved by extracting the kinetic energy from the water more gradually throughout the stroke. The original device was likely removing all momentum from the flow stream in the initial 1/3 of its stroke; by allowing the water to maintain more of its kinetic energy through the power extraction stroke, more energy should be

extracted by the wheel. Lastly, the waterwheel end panels have been replaced with a hub and spoke design to reduce the weight and moment of inertia of the device, which has been shown to improve performance, especially at lower flow speeds. [7] V1 and V2a prototypes are shown for direct comparison in Figure 13 below.

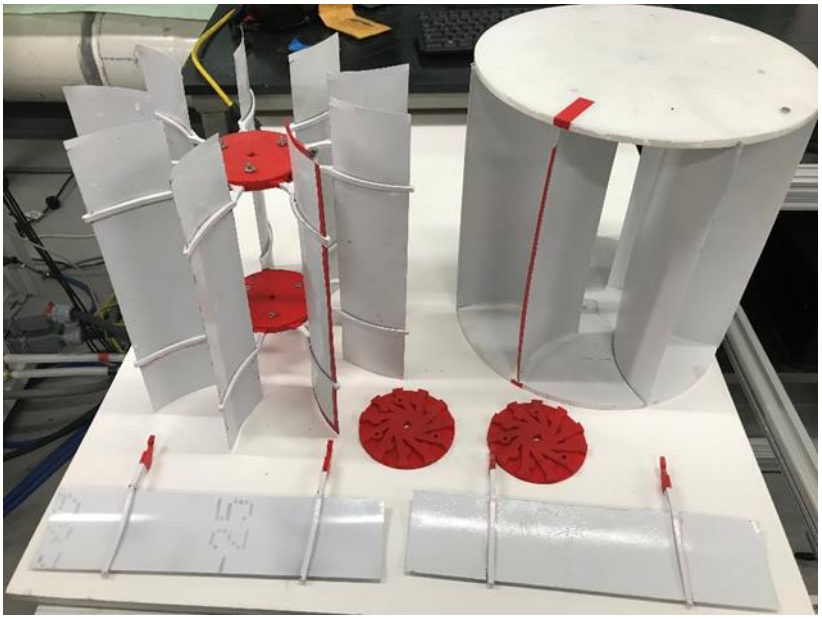

Figure 13 Comparison of V2a 9 Blade and V1 7 Blade Waterwheel Prototypes; 11 blade hubs and 2 additional blades also shown

The hub and spoke design features 3D printed components that snap together to assemble either the 9 or 11 blade wheels. Both versions have a width of 28 cm and diameter of 28 cm. The newer design also provides valuable insight into fabrication methods to be used for the full-scale device, with the intent of minimizing weight and incorporating the gearbox, generator and Power Take Off (PTO) components into a canister in the center of the wheel.

V2 Flow Concentrator:

Based on preliminary testing of the V1 concentrator prototype it was determined that the concentrator was most effective when the leading edge was placed slightly ahead of the wheel rather than directly beneath it and the space between the wheel and the device was minimized. The

V2 concentrator prototype was subsequently tested in various configurations in the FAU Wave Tank. The 1:5 scale prototype used for experimental testing is shown in Figure 14 below.

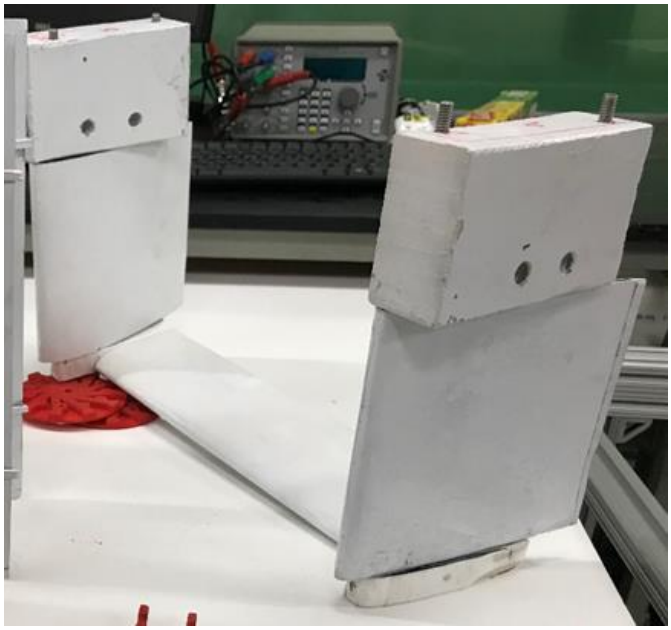

Figure 14 Version 2 Flow Concentrator (full device)

Three configurations have been investigated here: the full concentrator consisting of a 7.62 cm chord NACA 0018 bottom wing and two 15.24 cm chord NACA 4412 vertical side foils was tested in both forward (diffuser) and reverse (duct) position, followed by the more effective of these two configuration re-examined with the bottom wing removed. If the concentrator device offers comparable benefit to MHK performance without the bottom wing, it would be beneficial to remove this aspect of the design for the purposes of weight reduction and debris resistance. Furthermore, this would eliminate the risk of unbalanced lift forces impacting vessel buoyancy or stability. However, if it is determined that this aspect of the design is necessary, the components of lift force generated must be considered through the design process of the anchoring system, primarily in determining the mounting point at which the anchor line tension will be acting.

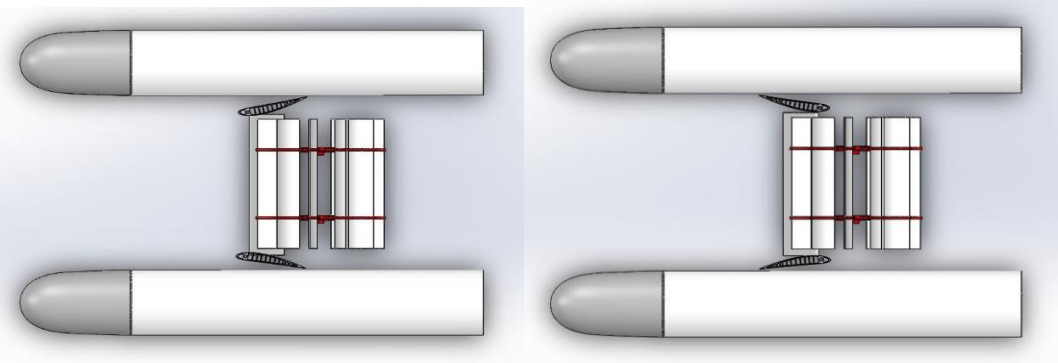

Figure 15 Forward (Diffuser) and Reverse (Duct) Position of Concentrator

Figure 15 above shows the forward (diffuser) and reverse (duct) positions of the concentrator. Based on previously conducted research and CFD analysis, it is expected that the forward (diffuser) position will be more effective. However, the reverse (duct) position is likely to be more resistant to debris, so if its performance is comparable, that would be the ideal configuration.

The full V2 testing setup shown in Figure 16 below consists of the waterwheel prototype (9 and 11 blade versions), 1:5 scale pontoons, flow concentrator and an Arduino based data acquisition system (DAQ) comprised of a magnetic hall sensor for RPM measurements and a load cell and torsion arm to measure applied torque.

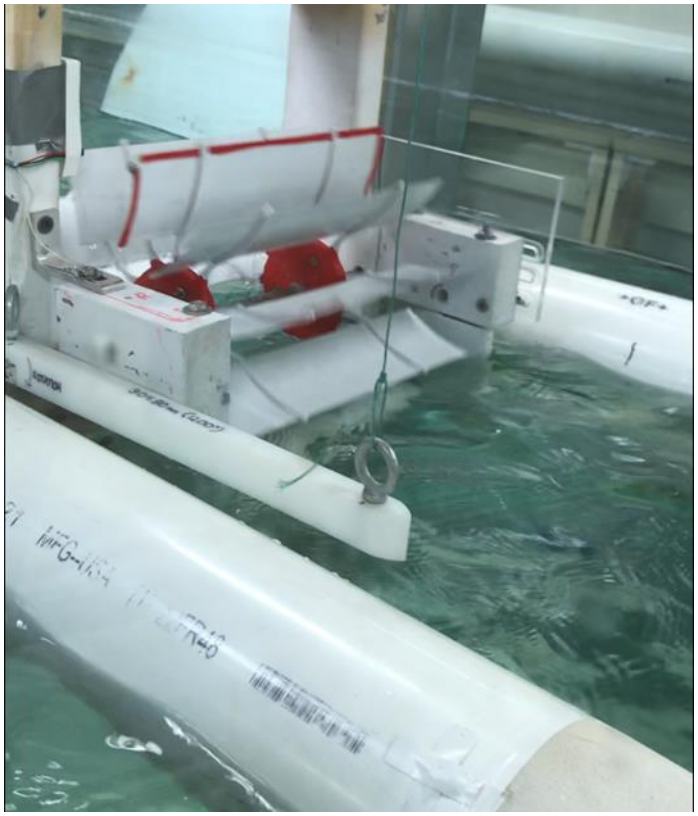

Figure 16 V2 Testing Configuration

The 1:5 scale PVC pontoons have been incorporated since V1 testing to more closely match the full-scale device conditions, with the MHK mounted at the rear of the vessel between the WAM-V pontoons. This modification facilitates a better understanding of the resulting flow patterns entering the waterwheel swept area and their effect on MHK performance.

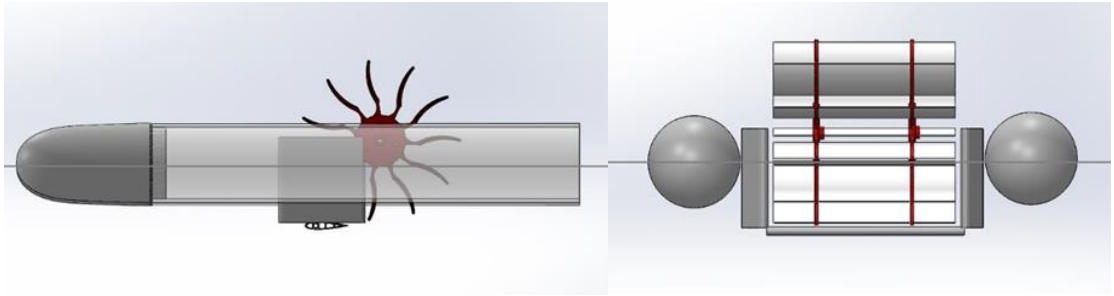

Figure 17 Side and Front View of Testing Setup

Figure 17 above shows the side and front view of the testing setup (neglecting mounting structures) with the waterline located at 33.3% of the waterwheel diameter and roughly 50% pontoon submergence. Based on V1 concentrator testing results, the assembly here aims to investigate the effects of varying the following key parameters.

Varying Gap:

The effect of varying the gap or spacing between the flow concentrator and waterwheel blades must be understood. As the most pronounced flow acceleration will occur in the boundary layers near the concentrator surface, it is imperative that the waterwheel is placed properly to make use of the accelerated region. An optimal spacing relative to the wheel diameter is therefore identified to inform full scale implementation.

Varying Wing Angle:

The effect of varying angle of attack of the device is another important characteristic to be examined. As demonstrated by the CFD analysis and Lift/Drag plots, the resulting flow field is highly dependent on hydrofoil angle. It is important to identify to what degree the waterwheel performance depends on concentrator angle.

Investigating Bottom Wing Impact:

Based on considerations beyond simply maximizing the device power coefficient, it may be beneficial to remove the bottom foil wing, relying solely on the side foils to concentrate the flow stream. One major concern for the bottom wing is unbalanced lift force generation. As shown in Table 4 below, the magnitude of lift forces generated at 1.5 m/s become quite large, even when the NACA 4412 wing has zero angle of attack due to its camber. A symmetric foil could reduce this effect, however there is no way to guarantee that no lift will be generated, as the attitude of the vessel shifts, the angle of attack will not remain neutral relative to the incoming flow.

Table 4: Lift Force estimates at full scale for NACA 4412 cambered hydrofoil

EQ: L=1/2*rho*A*Cl*U^2		NACA 4412 Cl @ 0 deg		NACA 4412 Cl @ 10 deg	
density (kg/m^2)	1025	0.35		1.25	
chord (m)	0.61				
width (m)	1.4	Lift Force			
		N	lbf	N	lbf
Flow Speed	0.25	9.57	2.15	34.19	7.69
	0.5	38.30	8.61	136.77	30.75
	0.75	86.17	19.37	307.74	69.18
	1	153.19	34.44	547.09	122.99
	1.25	239.35	53.81	854.83	192.17
	1.5	344.67	77.48	1230.96	276.72

Removing this aspect of the design will likely increase debris resistance of the system, while lowering induced drag and reducing potential environmental impact to marine wildlife. As shown in Figure 18, there is a much clearer path for surface debris to pass below the wheel without the risk of becoming caught between the blades and bottom wing.

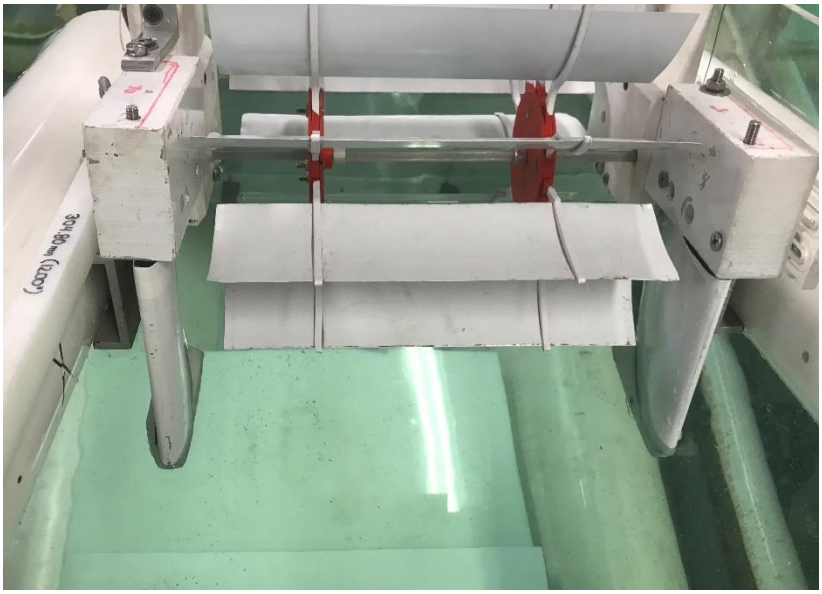

Figure 18: Front view of the waterwheel and flow concentrator with the bottom wing removed

Experimental Data Acquisition Setup:

For collecting experimental data, two different sensors are utilized for simultaneous measurement of the RPM and the applied load at the torsion brake. These sensors are attached to an Arduino Uno which is monitored via serial monitor and laptop. The wiring diagram in Figure 19 below shows the sensor connections to the Arduino Uno.

- Load Cell: Used for measuring force transferred from torsion brake attached to wheel axis
- Load Cell Amplifier: Uses signal from load cell and changes it to signal the Uno can read
- Hall Sensor and Magnet: A magnet is attached to the side of the wheel which passes by a hall sensor attached to the mounting structure. As the magnet passes the hall sensor a signal is sent to the Arduino that is used to calculate RPM based on the time interval between interrupts.

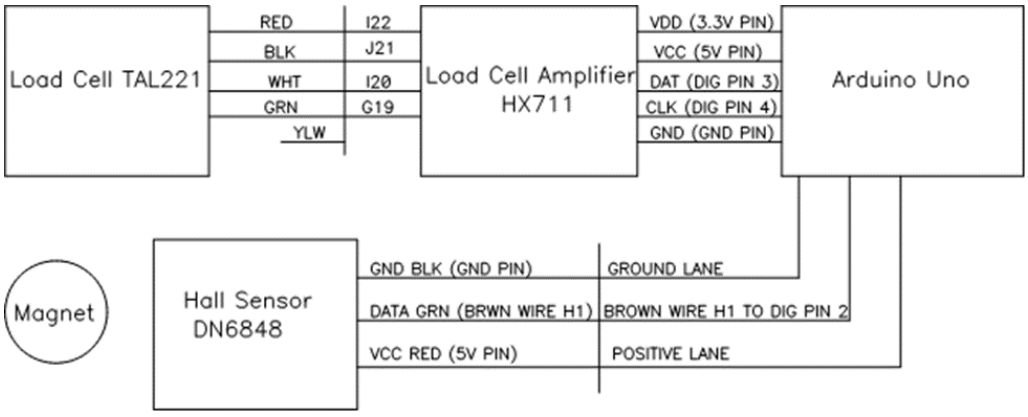

Figure 19 Wiring Diagram for Testing Setup

Data Acquisition Code:

There are two separate codes used for data collection. The first is the Calibration code used to tare the load cell. A calibration factor is obtained by suspending a known weight from the load cell and adjusting this factor until the correct weight is displayed in the serial monitor. The load cell must be calibrated prior to each testing cycle. The procedure for the main testing code is shown below:

1. Insert calibration factor into Testing Rig code
2. Attach interrupt to data pin from hall sensor. By attaching the interrupt to this pin, if a magnet passes by the hall sensor it's registered as an interrupt and the signal falls from 1 to 0.
3. Tare the load cell with no weight applied
4. If no interrupt is detected, the load from the load cell is displayed on the serial monitor in grams
5. If the magnet passes by the hall sensor and an interrupt is detected by the Arduino, the difference between the time for the last interrupt detected is used to calculate the RPM. The load is also displayed at the same time.

The basic code logic is outlined below in Figure 20, with the full code used for experimental data collection included in the Appendix.

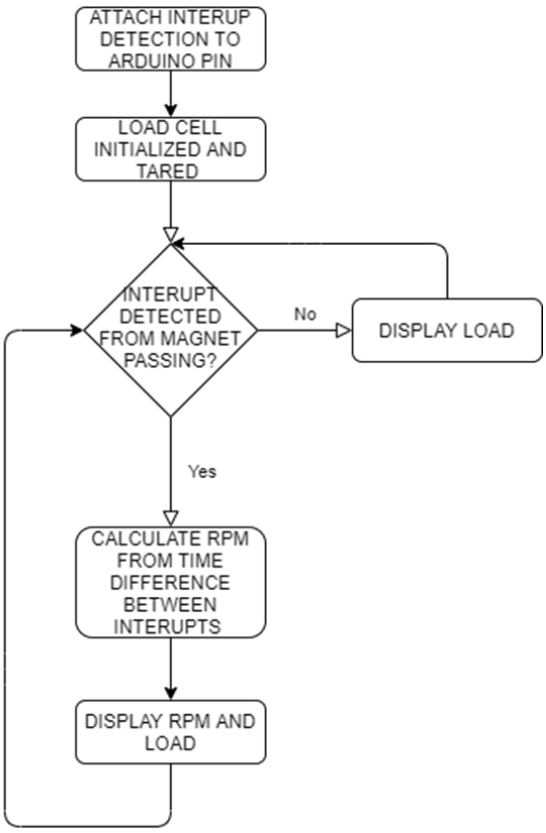

Figure 20 Code Logic for Testing Setup

RESULTS

Preliminary CFD Results:

Results obtained by the ANSYS CFX solver include pressure and velocity contours surrounding the concentrator designs. These preliminary results provided valuable insight into the flow fields surrounding hydrofoil shapes particularly in understanding the magnitude and locus of acceleration imparted on the fluid velocity for various cases. The simulation results shown below (Fig 21-24) included an inlet velocity of 0.5 m/s and the NACA 4412 profile, with 15.24 cm chord length and 30.48 cm width set to a 10° angle of attack which was percieved to be the optimal angle based on the lift/drag polars found in [10]. As seen in Figure 21, the highest pressure on the surface of the concentrator is developed along the leading edge near the stagnation point. This region of roughly 101.45 kPa (when using 1 atm as the reference pressure) is where the majority of the drag force is developed, according to the fundamental relation in Eq. 15. The top (suction) side of the foil profile develops low pressure of 101.11 kPa while the bottom (pressure) side has relatively uniform pressure distribution with a magnitude of approximately 101.35 kPa. This result is in agreement with the expected pressure distribution as discussed in the Background section.

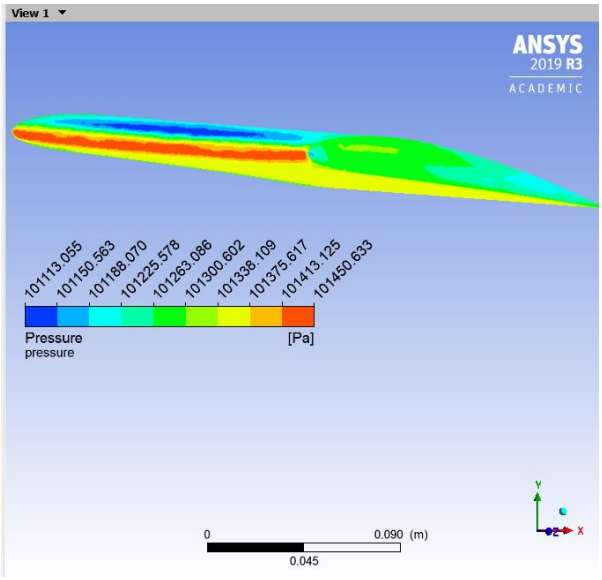

Figure 21: Surface pressure contour along the foil profile with 1 atm (101.325 kPa) reference pressure

The pressure distribution within the surrounding fluid is examined by defining a mid-section plane with a variable pressure contour. The side-view in Figure 22 shows the low-pressure fluid region developed along the top face of the foil and the high-pressure region developed along the bottom/leading edge.

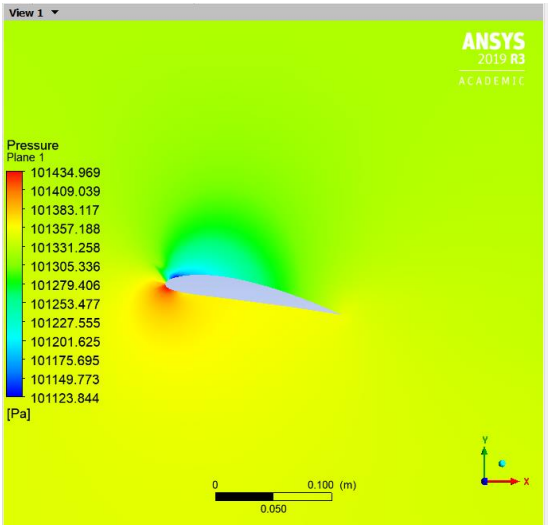

Figure 22: Surrounding fluid pressure contour with 1 atm (101.325 kPa) reference pressure, 10° AOA with 0.5 m/s flow velocity

Particle streamlines provide another way to visualize the flow regime around the hydrofoil. Using a 2-D surface streamline applied to a mid-plane with 1000 equally spaced particles, the flow surrounding the foil is captured well. Figure 23 below is generated by applying a variable color based on particle velocity to the stream lines. It can be seen that the flow velocity is increased from the inlet speed of 0.5 m/s to approximately 0.75 m/s (150% increase) within a localized region along the suction side of the foil.

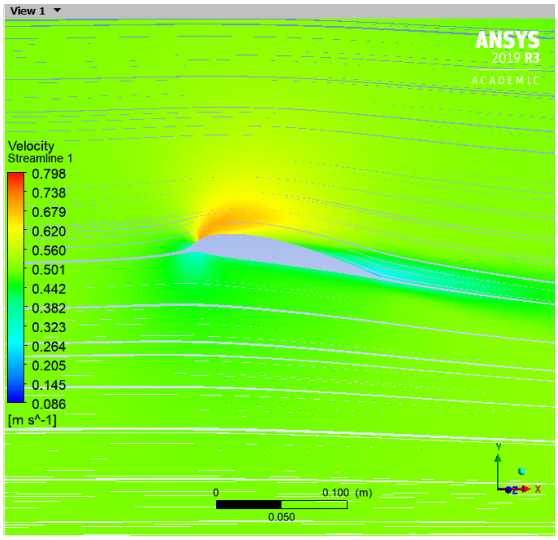

Figure 23: Particle velocity streamlines, 10° AOA with 0.5 m/s inlet velocity.

A front view shown in Figure 24 shows that this velocity distribution is uniform along the length of the concentrator, with slightly less acceleration near the ends where the water particles are free to move around the wing.

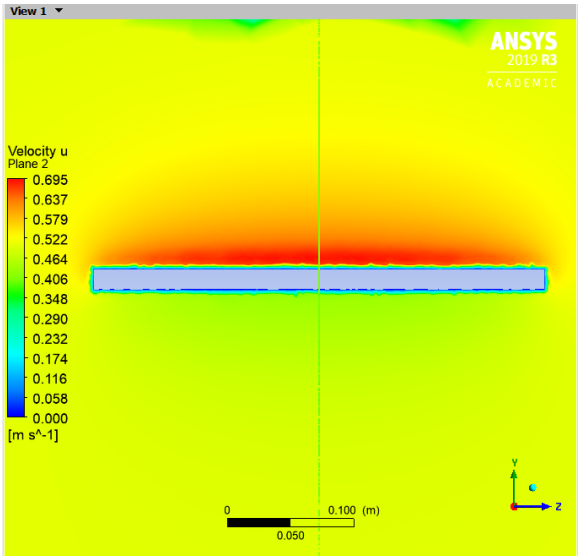

Figure 24: Front View of velocity contour, 10° AOA with inlet velocity of 0.5 m/s

Upon examining the results above, it becomes clear that additional entrainment of the flow may likely be possible. The geometry of the waterwheel allows for the concentrator to more completely surround the submerged blades, and therefore an adaptation with hydrofoil sides is investigated

The velocity contour in Figure 25 shows the concentrator with the same NACA 4412 foil shape and 10° angle of attack in a vertical orientation as the sides of the device. This result shows more prominent acceleration in the desired region. By constraining the flow from the sides, this configuration allows for a much larger accelerated region than the open side configuration.

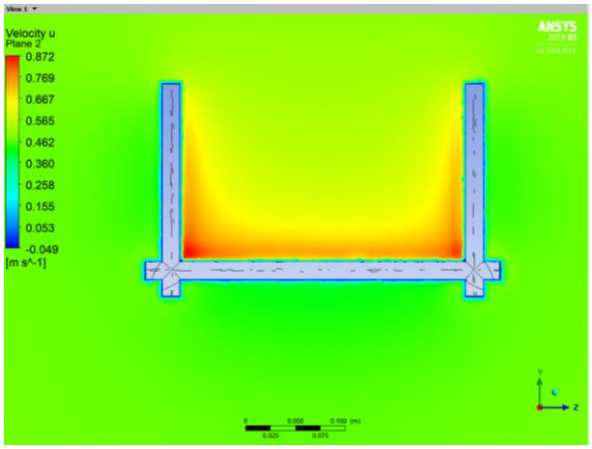

Figure 25: Front view velocity contours of concentrator with 10° AOA NACA foil sides

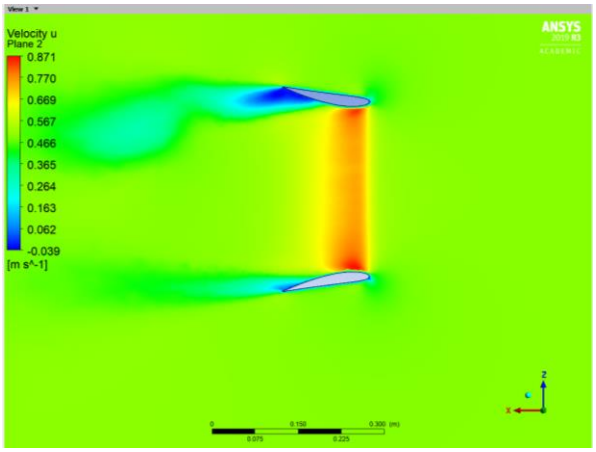

Figure 26: Top view velocity contours of concentrator with 10° AOA NACA foil sides

When comparing the results in Figures 22/23 & 25/27 it is noted that the pressure and velocity distributions are essentially inverses of one another, as is to be expected based on Eq. 9.

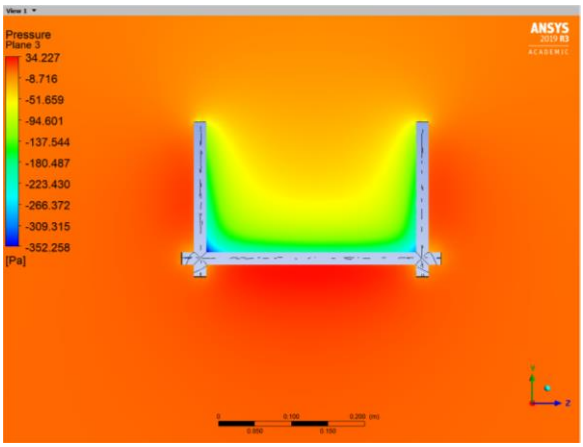

Figure 27: Top view pressure contours of concentrator with 10° AOA NACA foil sides (0 Pa used as reference pressure)

Experimental Results:

V1 Tank Testing:

The V1 Prototype waterwheel and flow concentrator were tested in the FAU wave tank over a water velocity range of 0.359 - 0.502 m/s, dictated by the device startup speed and maximum tank setting. The results for the 15 positions investigated initially are summarized in Table 5 below.

Table 5: Max Measured Power Coefficients for initial testing phase.at 0.502 m/s flow speed Note: at this flow speed, open wheel CP=0.122

Horizontal Position	Vertical Position	Wing Angle (deg)	Gap Size (cm)	CP max
Forward	Top	10	1	0.129
		0	0.5	0.134
		-10	0.5	0.133
Forward	Middle	10	2	0.125
		0	1.5	0.128
		-10	1	0.13
Middle	Middle	10	1	0.129
		0	0.5	0.135
		-10	0.5	0.133
Middle	Low	10	3	0.124
		0	2.5	0.122
		-10	2	0.122
Rear	Middle	10	2.5	0.122
		0	2	0.121
		-10	1.5	0.123

Based on these results, it can be deduced that the most important factor in determining performance is the spacing between the concentrator foil and the waterwheel blades. A steep drop in performance boost was noticed for any tests with spacing larger than 1.5 cm, while all tests with a gap of <1 cm showed similar levels of positive impact, regardless of foil angle. The forward position outperformed the rear, suggesting that the device should be placed ahead of the wheel for optimal impact. The effect of positive angle (diffuser) vs negative angle (Duct) is examined further in the second testing phase, where both cases aim to minimize gap spacing.

In examining power output characteristics, it is most beneficial to view the results in terms of power coefficient as a function of tip speed ratio. Figure 28 below summarizes the testing results of the 7-blade wheel with and without the V1 concentrator in place.

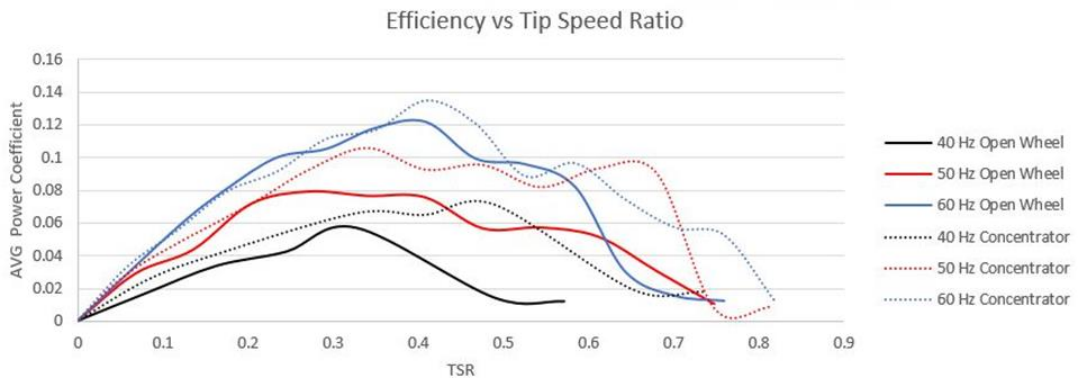

Figure 28 Efficiency vs Tip Speed Ratio for MHK

As seen here, the optimal tip speed ratio for the device was determined to be approximately 0.4. The maximum power coefficient achieved was roughly 0.135 with the concentrator in place, at a flow velocity of 0.502 m/s. The results in Table 6 below show that the most prominent increase in power coefficient offered by the concentrator correspond to lower flow speeds.

Table 6: Results summary from V1 waterwheel and flow concentrator tank testing

7 Blade Waterwheel		Flow Speed m/s		
		0.359	0.431	0.502
Max AVG Power Coefficient	Open Wheel	0.057	0.080	0.122
	With Concentrator	0.071	0.106	0.135
	Percent Increase	25.00%	32.83%	10.50%

V2 Tank Testing:

The 9 and 11 blade V2 prototypes outperformed the 7 blade V1 prototype significantly. The average maximum power coefficient measured for each device verses flow speed appear in Figure 29. It is also worth noting that the V2 prototypes began rotating at much lower flow velocities, producing some power at flow speeds as low as 0.16 m/s, compared to the 0.35 m/s startup speed of the original prototype.

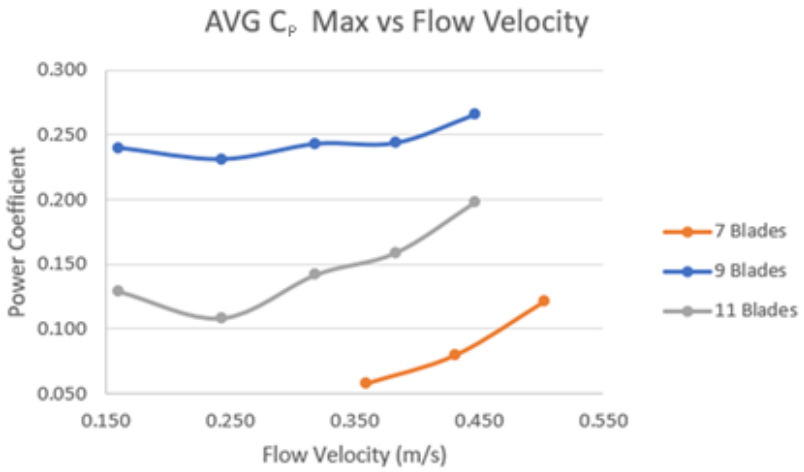

Figure 29 Average C_P Max vs Flow Velocity of Prototype Wheels

Figure 29 above shows the measured power coefficient vs flow speed for the three USWW prototypes. Based on these results, the 9 Blade prototype is the most efficient, reaching a C_P max of approximately 0.27; a 107% increase in mechanical efficiency when compared to the V1 prototype C_P max.

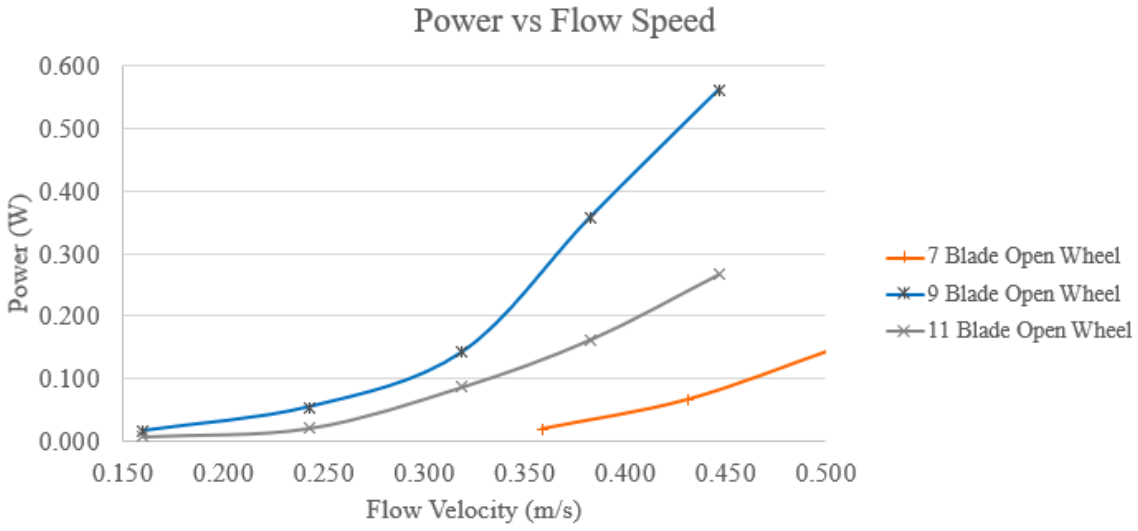

Figure 30 Prototype Power Output vs Flow Speed

Figure 30 above shows the magnitude of power output at the prototype scale as a function of flow speed. Due to the combined effects of increased capture area and increased efficiency, the total output of the USWW is significantly improved.

While the 9-blade prototype was the most efficient open wheel, the results including the concentrator showed no notable increase in power coefficient. Additionally, as seen in Figure 31 below, some of the dataset trends are uncharacteristic, i.e displaying a linear trend or negative values.

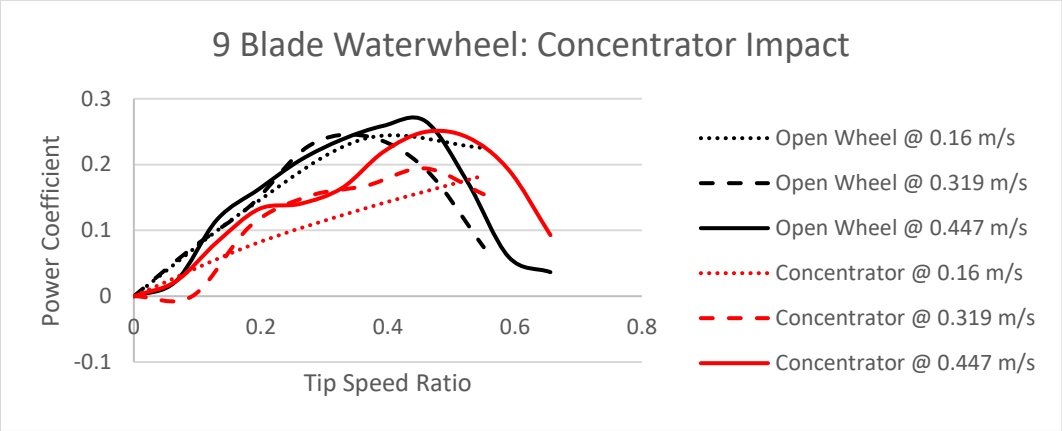

Figure 31: Concentrator impact on 9-blade waterwheel

Whether the lack of measured performance increase for the 9-blade wheel was due to measurement error or simply a function of the wheel geometry remains somewhat unclear. Nevertheless, the results for the 11-blade wheel show a much more pronounced improvement and more consistent trends. Therefore, the main focus will be placed on examination of the concentrator testing results for the 11-blade waterwheel. The concentrator testing results for the 11-blade V2b prototype are summarized below in Figure 32.

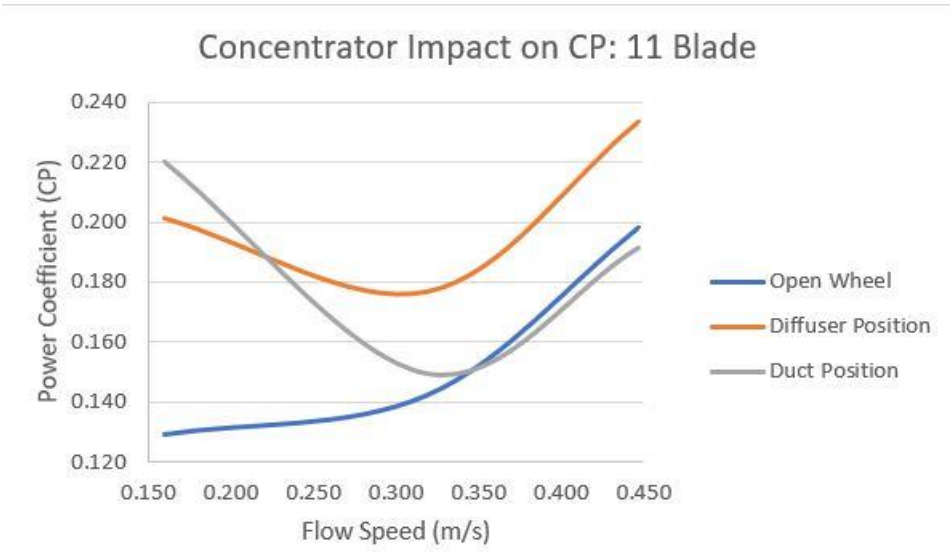

Figure 32 11-Blade Concentrator CP Results

Based on these results, the forward (diffuser) configuration is most effective. Both concentrator configurations produce a significant increase in power coefficient at very low flow speeds, however, it is observed that the diffuser position significantly outperforms the open wheel and duct positions closer to the target speed of 0.5 m/s.

Flow Speed	Open Wheel			Full Forward					Full Reverse				
	AVG Power	AVG CP	CP Max	AVG Power	AVG CP	AVG % Increase	CP Max	MAX % Increase	AVG Power	AVG CP	AVG % Increase	CP Max	Max % Increase
0.160	0.007	0.129	0.144	0.011	0.201	55.96	0.302	109.0	0.008	0.220	70.64	0.310	114.75
0.319	0.060	0.142	0.207	0.074	0.177	24.33	0.266	28.42	0.063	0.150	5.349	0.398	92.09
0.447	0.228	0.198	0.231	0.269	0.233	17.85	0.436	88.37	0.221	0.191	-3.298	0.271	17.32

Table 7 Flow Speeds and Cp performances

As shown in above, the reverse (duct) configuration offered a 70% increase in C_P at the startup flow speed of 0.16 m/s, however its power coefficient was 3% lower than the open waterwheel at higher flow speeds. This is likely caused by water "piling up" at higher velocities due to a buildup of positive pressure ahead of the device, rather than the water being pulled through the capture plane by a low-pressure region behind it. A similar effect was noted in the findings presented by Cleynen, Olivier, et al. [7] for waterwheels with excessive submergence. The forward (diffuser)

configuration provides a 55% increase in C_P at 0.16 m/s and nearly 18% increase at 0.447 m/s, making it the obvious choice. Experimental studies conducted by Chihaia, Rareş-Andrei, et al. [5], Maulana, Muhammad Ilham, et al. [19] and Ohya, Yuji, and Takashi Karasudani. [23] which compared the effectiveness of duct and diffuser based augmentation devices also determined that the diffuser was a more effective tactic in increasing the power capture and efficiency of their respective energy harvesting devices.

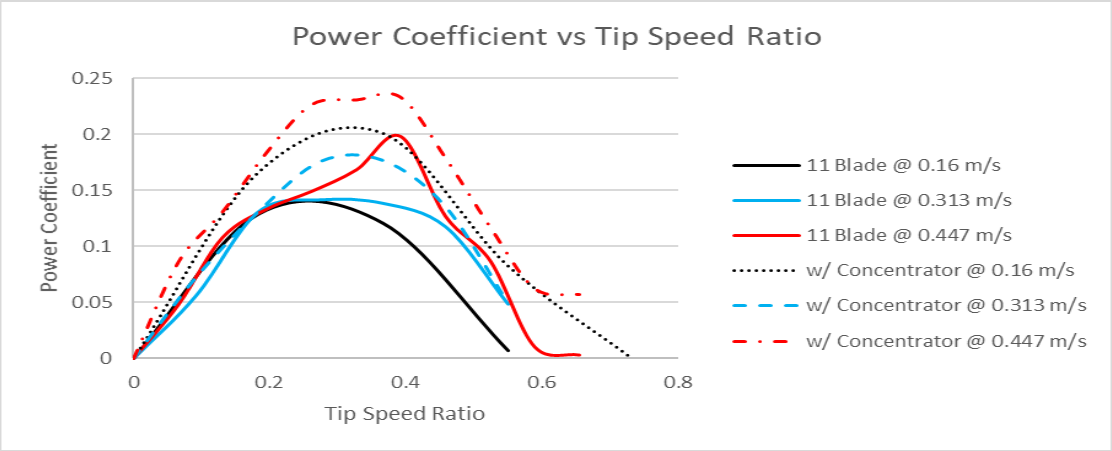

Figure 33 Power Coefficient vs Tip Speed Ratio curves for the 11-blade wheel with and without the flow concentrator in forward (diffuser) position

The results in Figure 33 for the 11-blade wheel with and without the concentrator in forward (diffuser) position show that again, the maximum power coefficient is measured at a tip speed ratio (TSR) of roughly 0.4. While this result varies slightly between datasets, most testing results presented a C_P max at a TSR between 0.3 and 0.5. These results are in agreement with the findings presented by Cleynen, Olivier, et al. [7], who measured experimentally and predicted with 3D simulation, performance of a 30-cm diameter water wheel model with 10 blades, incoming velocity U= 0:67 m/s, and 33% of the wheel radius immersed in the water. Their work measured a max power coefficient of approximately 0.39 at a tip speed ratio of 0.5.

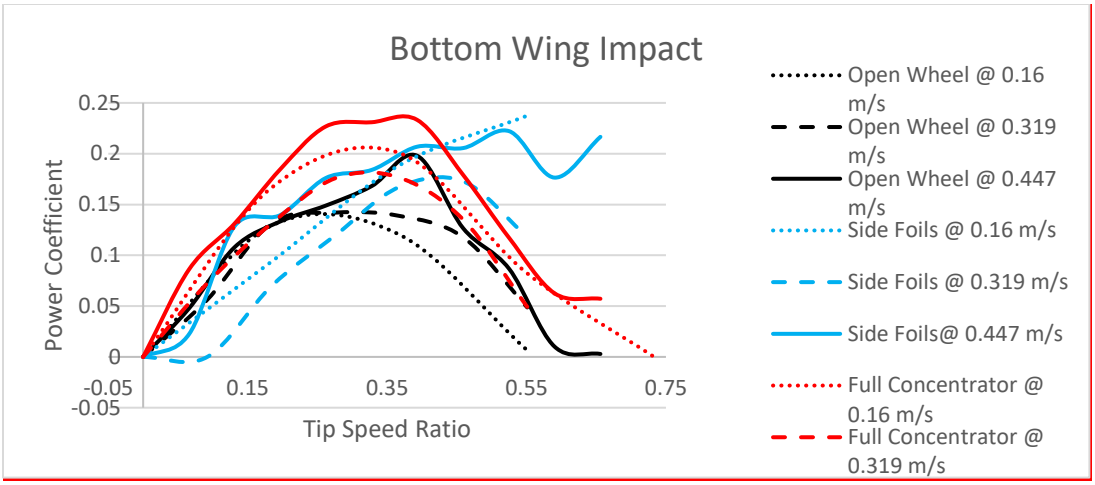

Figure 34: Concentrator impact on measured Power Coefficient for V2b 11-blade prototype

The performance of the concentrator with the bottom wing removed has been investigated for the V2b 11 blade wheel, with results shown in Figure 34 above. This configuration offers some benefit compared to the open wheel, with notably higher CP values at higher tip speed ratios (TSR = 0.45-0.65).

Table 8: Summarized testing results for the 11-blade waterwheel and concentrator with side foils only, ie. bottom wing removed

Flow Speed	Open Wheel		Full Forward (Diffuser)				Sides Only			
	AVG CP	CP Max	AVG CP	AVG % Increase	CP Max	MAX % Increase	AVG CP	AVG % Increase	CP Max	MAX % Increase
0.160	0.13	0.14	0.20	56.0	0.30	109.0	0.24	83.9	0.31	136.7
0.319	0.14	0.21	0.18	24.3	0.27	28.4	0.17	21.7	0.47	232.0
0.447	0.20	0.23	0.23	17.8	0.44	88.4	0.22	12.2	0.26	30.4

Based on the results summarized above, the performance of the flow concentrator with the side foils only is deemed sufficient, producing at least 94% of the performance increase offered by the full device at all flow speeds, and outperforming the full concentrator Cp at 0.16 m/s by nearly 50%. It is likely that this configuration of the flow concentrator maintains most of the effectiveness of the full device because the accelerated region generated by the vertical foil wings is in contact with the passing blades for a longer duration within their power stroke. The accelerated region

generated by the bottom wing, while spanning the entire width of the wheel, was only being utilized by a single blade passing close enough to enter the boundary layer at a time.

Full Scale Performance:

Scaling Power Coefficient:

The full-scale device power coefficients can be estimated using the Reynold's Scaling method, as is common practice in hydro- and aerodynamic prototype testing procedures. [21] A scale factor of 1:5 between the prototype and full-scale characteristic length is used to equate the Reynold's number (non-dimensional velocity) present in each flow condition.

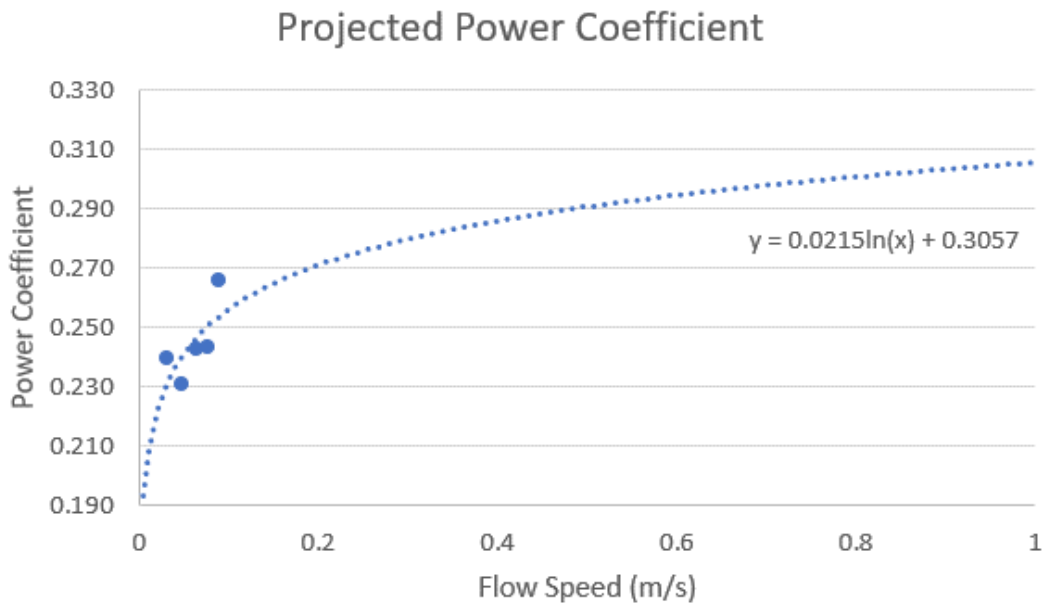

Figure 35: Projected Power Coefficients based on 1:5 Reynold's scaling

Figure 35 shows a logarithmic curve fit to the datapoints from the V2b Prototype wheel testing results. By forecasting the CP values in this manner, the coefficients for corresponding Reynold's numbers can be equated so that the Cp value at 0.5 m/s at the prototype scale corresponds to the full-scale device Cp at 0.1 m/s and so forth.

Projecting Power Output:

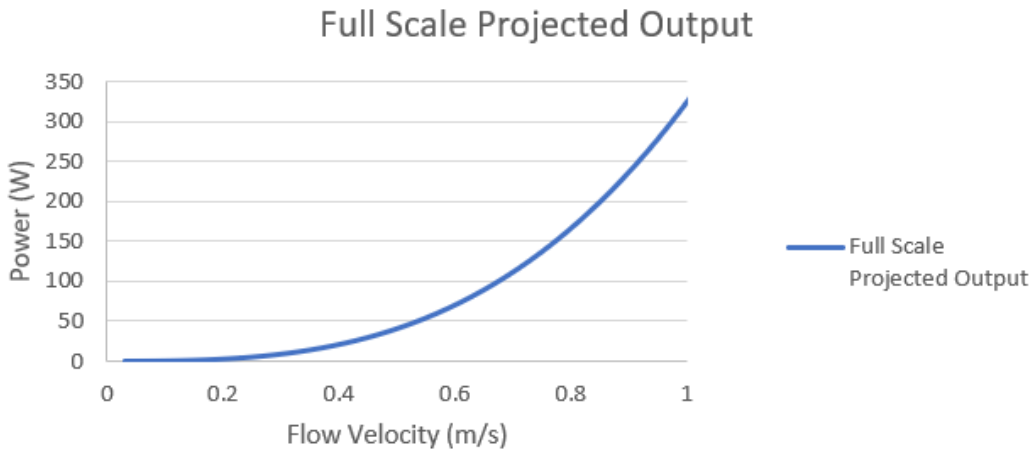

Figure 36: Power Output Estimates for Full Scale MHK Device

Using the Reynold's scaled power coefficient estimates from Figure 35 and the full scale device capture area, the power output of the full-scale USWW (55in width x 37 in diameter) is estimated and shown in Figure 36 for flow speeds from 0 - 1 m/s. The mechanical power output of the wheel at the target current velocity of 0.5 m/s is approximately 40 W, while the device is expected to reach 300 W of mechanical power production just below 1 m/s flow velocity.

Additional Considerations:

Further investigation into debris interactions between the waterwheel, flow concentrator, and pontoons is recommended. Testing with representative models for various types of surface debris that is likely to interact with the MHK including plastic bags, coconuts, fishing line/nets etc. will be beneficial in identifying and mitigating the potential environmental risks to the system. For example, an adaptation such as a rubberized flap to seal the gap between the concentrator and pontoons could be an effective solution if it was observed that debris was becoming lodged in that location. Lastly, as the research project approaches implementation of the full-scale system, attention should be paid to the mounting and deployment structure, as it is yet unclear how the articulation of the vessel during operation will impact clearance of the deployed MHK subsystem.

Conclusions:

Based on the experimental findings of this report, it is indeed possible to improve the power output and efficiency of a floating waterwheel by locally modifying the flow regime across the power capture plane. By inserting a streamlined device with proper dimensions and placement, the amount of kinetic energy extracted from the entrained water volume by the MHK can be increased significantly. The most effective device configuration examined here was the full device in forward (diffuser) position. The inclusion of the flow concentrator offered a 17-55% increase in measured power coefficient during tank testing conducted over a range of 0.16 - 0.447 m/s flow speed. The effectiveness of the flow concentrator is noted to be highest at lower flow speeds, a characteristic that will be beneficial for startup and power production of the full-scale device at low flow speeds. Some adaptation to the concentrator design may be needed as the DOE research project approaches full-scale implementation of the system. Areas for possible improvement and design alterations include investigating debris resistance of the deployed device and finalizing mounting structures to ensure proper clearance between the pontoons and waterwheel when fixed to the articulating platform structure.

APPENDICES

ANSYS Waterwheel Simulation:

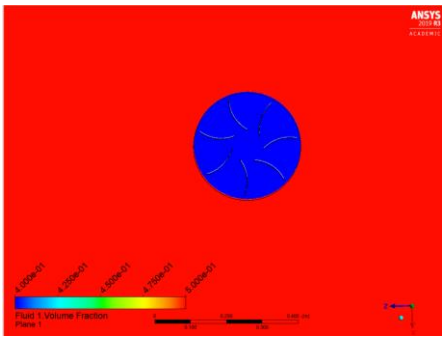

Initial timestep, showing volume fractions of water: 0.5 for stationary domain and 0.4 for rotating subdomain.

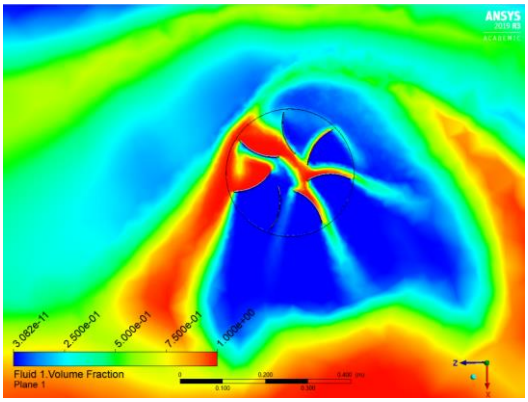

Timestep #10, fluid separation stage.

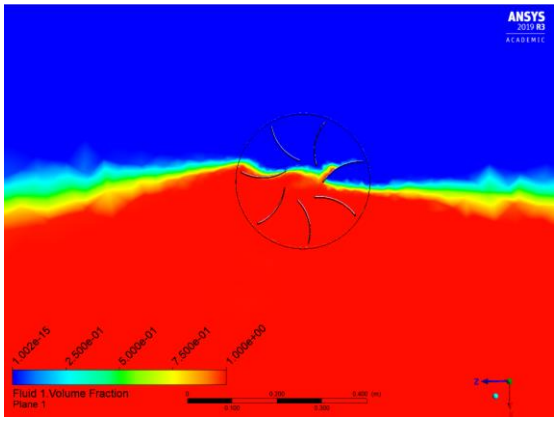

Timestep #30, fluid separation complete

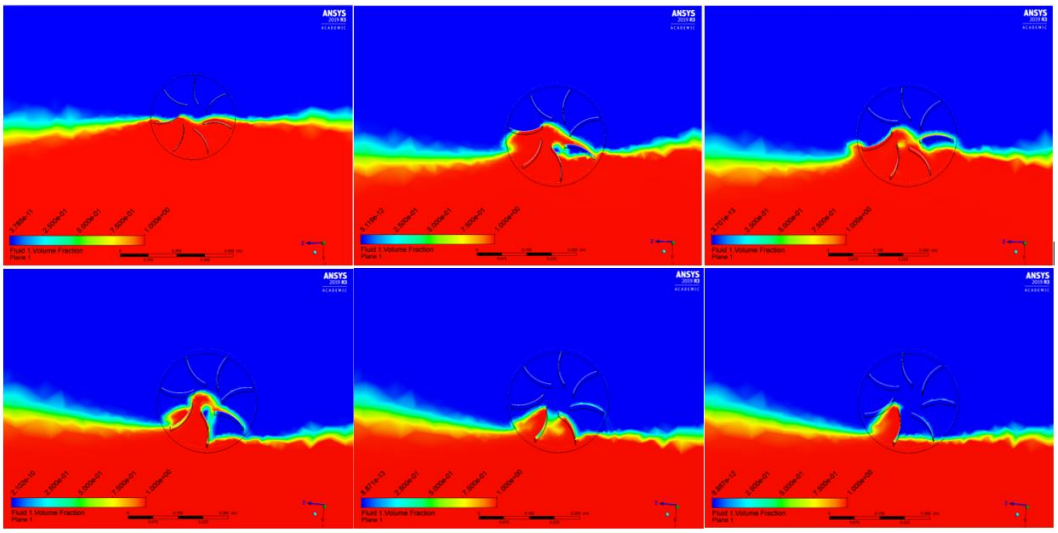

Water volume fraction variation during simulation. Top (left-right) Timestep #50, 75, 95, Bottom (left – right) Timestep #105, 115, 125

ANSYS CFX Towque Monitor:

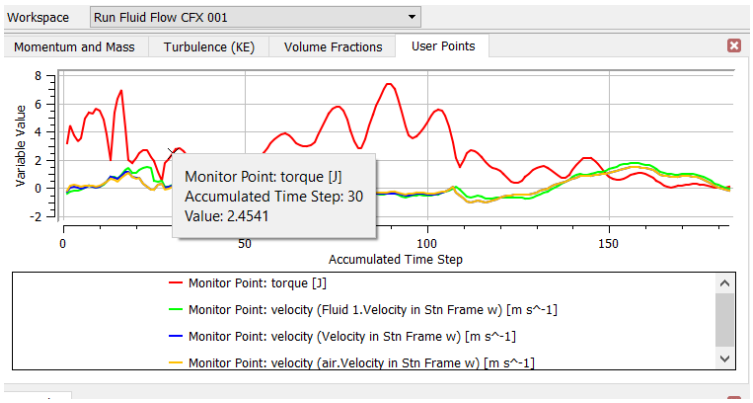

DAQ Code:

TestingRig.ino | Arduino 1.8.13

File Edit Sketch Tools Help

TestingRig.ino §

```
#include "HX711.h"
#define calibration_factor 15700 //This value is obtained using the SparkFun_HX711_Calibration sketch you have to do this again for each test
#define DOUT  3
#define CLK  4
const int interruptPin = 2;
volatile byte full_revolutions = 0;
int rpm = 0;
unsigned long timeold = 0;
HX711 scale;
void setup()
{
  Serial.begin(115200);
  pinMode(interruptPin, INPUT_PULLUP);
  Serial.println("HX711 scale demo");
  attachInterrupt(digitalPinToInterrupt(interruptPin), magnet_detect, FALLING);//Initialize the intterrupt pin (Arduino digital pin 2)

  scale.begin(DOUT, CLK);
  scale.set_scale(calibration_factor); //This value is obtained by using the SparkFun_HX711_Calibration sketch
  scale.tare(); //Assuming there is no weight on the scale at start up, reset the scale to 0
  Serial.println("Readings:");
}
void loop()
{

    if (full_revolutions >= 1) {
    rpm = 30*1000/(millis() - timeold)*full_revolutions;
    rpm = rpm *2;
    timeold = millis();
    full_revolutions = 0;
    Serial.print("RPM:  ");
    Serial.print(rpm);
    Serial.print("    Scale:  ");
    Serial.println(scale.get_units(), 1);
    }
    else (full_revolutions = 0);{
//      full_revolutions = 0;
        Serial.print("    Scale:  ");
    Serial.println(scale.get_units(), 1);
    }
}

 void magnet_detect() //Called whenever a magnet/interrupt is detected by the arduino
 {
   full_revolutions++;

 }
```

CFD Power Estimate: (Impossibly high; CP > 1)

Inlet Velocity: 0.5 m/s				Wheel RPM: 10				Wheel rad/s (ω):				1.05	Power Calculated using: P=Txω							AVG
Timestep	30	35	40	45	50	55	60	65	70	75	80	85	90	95	100	105	110	115	120	
Torque (Nm)	2.45	1.95	1.23	1.07	1.15	2.46	3.79	3.02	3.76	5.79	3.29	5.22	7.37	3.7	4.63	5.12	1.73	2.21	1.19	3.22
Power (W)	2.57	2.05	1.29	1.12	1.21	2.58	3.98	3.17	3.95	6.08	3.45	5.48	7.74	3.9	4.86	5.38	1.82	2.32	1.25	3.38

REFERENCES

[1] *AIAA Guide for the Verification and Validation of Computational Fluid Dynamics Simulations*. American Institute of Aeronautics and Astronautics, 1998.

[2] "ANSYS CFX: Pre-User's Guide." *ANSYS.com*, ANSYS Inc., read.pudn.com/downloads500/ebook/2077964/cfx_pre.pdf.

[3] Bachant, Peter, and Martin Wosnik. "Effects of Reynolds Number on the Energy Conversion and ..." *MDPI*, 2016, www.mdpi.com/1996-1073/9/2/73/pdf.

[4] "CFD Online." Online.com, www.cfd-online.com/

[5] Chihaia, Rareş-Andrei, et al. "Increasing the Energy Conversion Efficiency for Shrouded Hydrokinetic Turbines Using Experimental Analysis on a Scale Model." *E3S Web of Conferences*, vol. 85, 2019, p. 06004., doi:10.1051/e3sconf/20198506004.

[6] CHORIN, ALEXANDRE JOEL. *Numerical Solution of the Navier-Stokes Equations for an Incompressible Fluid (Classic Reprint)*. FORGOTTEN Books, 2015.

[7] Cleynen, Olivier, et al. "Characterization of the Performance of a Free-Stream Water Wheel Using Computational Fluid Dynamics." *Energy*, Pergamon, 19 Oct. 2018, www.sciencedirect.com/science/article/pii/S0360544218319844.

[8] Davidson, Peter. *Turbulence: for Mathematics and Engineering*. Oxford University Press, 2004.

[9] Fletcher, C. A. J. *Computational Techniques for Fluid Dynamics. Fundamental and General Techniques*. Springer-Verlag, 1991.

[10] Goswami, D. Yogi, and Frank Kreith. *Energy Conversion*. CRC Press, Taylor & Francis Group, 2017.

[11] Haberman, Richard. *Applied Partial Differential Equations 5th ed*.

[12] Khan, M.j., et al. "Hydrokinetic Energy Conversion Systems and Assessment of Horizontal and Vertical Axis Turbines for River and Tidal Applications: A Technology Status Review." *Applied Energy*, vol. 86, no. 10, 2009, pp. 1823–1835., doi:10.1016/j.apenergy.2009.02.017.

[13] Landau, L. D., and E. M. Lifshitz. *Fluid Mechanics*. Elsevier, 2004.

[14] "Lift & Drag Polars." *Airfoil Lift and Drag Polar Diagrams*, Airfoiltools.com, airfoiltools.com/polar/details?r=polar%2Findex%2F#xfoil.

[15] Lisejkin, Vladimir D. *Grid Generation Methods*. Springer Netherland, 2009.

[16] Logan, Daryl L. *A First Course in the Finite Element Method*. Cengage Learning, 2017.

[17] Mannion, Brian, et al. "An Experimental Study of a Flow-Accelerating Hydrokinetic Device." *Proceedings of the Institution of Mechanical Engineers, Part A: Journal of Power and Energy*, vol. 233, no. 1, 2018, pp. 148–162., doi:10.1177/0957650918772626.

[18] Manwell, J. F., et al. *Wind Energy Explained: Theory, Design and Application*. John Wiley & Sons, 2011.

[19] Maulana, Muhammad Ilham, et al. "Analysis of Diffuser Augmented Wind Turbine (DAWT) with Flange and Curved Interior Using CFD." 2018, doi:10.1063/1.5046609.

[20] Muller, Kolja. "IMPROVED TANK TEST PROCEDURES FOR SCALED FLOATING OFFSHORE WIND TURBINES." *International Wind Engineering ConferenceElib.uni-Stuttgart.de/Bitstream/11682/8278/1/Mueller2014_Improved_Tank_Test_Procedures_For_Floating_Offshore_Wind_Turbines.Pdf*, 2014, elib.uni-stuttgart.de/bitstream/11682/8278/1/Mueller2014_Improved_Tank_Test_Procedures_For_Floating_Offshore_Wind_Turbines.pdf.

[21] Multon, Bernard. *Marine Renewable Energy Handbook*. ISTE, 2012.

[22] "NACA 4412 Airfoil Details." *NACA 4412 (naca4412-Il)*, Airfoiltools.com, airfoiltools.com/airfoil/details?airfoil=naca4412-il.

[23] Ohya, Yuji, and Takashi Karasudani. "A Shrouded Wind Turbine Generating High Output Power with Wind-Lens Technology." *Energies*, vol. 3, no. 4, 2010, pp. 634–649., doi:10.3390/en3040634.

[24] Plewa, Thomasz. *Adaptive Mesh Refinement: Theory and Applications*. Springer, 2005.

[25] Press, William H. *Numerical Recipes in C++: the Art of Scientific Computing*. Cambridge Univ. Press India, 2007.

[26] Quaranta, Emanuele, and Roberto Revelli. "CFD Simulations to Optimize the Blade Design of Water Wheels." *Drinking Water Engineering and Science*, vol. 10, no. 1, 2017, pp. 27–32., doi:10.5194/dwes-10-27-2017.

[27] Quaranta E. "Investigation and optimization of the performance of gravity waterwheels." Ph.D. thesis. Politecnicodi Torino; 2017.https://core.ac.uk/download/pdf/84252843.pdf

[28] Rogallo, Robert S. *Numerical Experiments in Homogeneous Turbulence*. National Aeronautics and Space Administration, 1981.

[29] Schultz, M. P., and K. A. Flack. "Reynolds-Number Scaling of Turbulent Channel Flow." *AIP Publishing*, American Institute of PhysicsAIP, 1 Jan. 1970, aip.scitation.org/doi/full/10.1063/1.4791606.

[30] Sornes, Kari. "Small-Scale Water Turbines for River ApplicationsKari." *Zero.no*, zero.no/wp-content/uploads/2016/05/small-scale-water-current-turbines-for-river-applications.pdf.

[31] Stringer, R.M., et al. "Numerical Investigation of Laboratory Tested Cross-Flow Tidal Turbines and Reynolds Number Scaling." *Renewable Energy*, Pergamon, 15 Aug. 2015, www.sciencedirect.com/science/article/pii/S0960148115301774.

[32] Tennekes, Hendrik, and John L. Lumley. *A First Course in Turbulence*. MIT Press, 2006.

[33] Thompson, Joe F., et al. *Handbook of Grid Generation*. CRC Press, 1999.

[34] White, F. M. *Viscous Fluid Flow*. McGraw-Hill, 2006.

[35] Zhao, Mengshang, et al. “Ects on a Water Wheel Using Experimental and Numerical ...” *MDPI*, Mar. 2020, www.mdpi.com/2073-4441/12/4/982/pdf.

[36] Zikanov, Oleg. *Essential Computational Fluid Dynamics*. John Wiley & Sons, Inc., 2019.